Development/Plasticity/Repair

Posthearing Ca^{2+} Currents and Their Roles in Shaping the Different Modes of Firing of Spiral Ganglion Neurons

Ping Lv,[1,2] Choong-Ryoul Sihn,[2] Wenying Wang,[2] Haitao Shen,[1] Hyo Jeong Kim,[2] Sonia M. Rocha-Sanchez,[3] and Ebenezer N. Yamoah[2]

[1]The Key Laboratory of Neural and Vascular Biology, Ministry of Education, Hebei Medical University, Shijiazhuang, China 050017, [2]University of California, Davis, School of Medicine, Center for Neuroscience, Program in Communication Science, Davis, California 95618, and [3]Creighton University School of Dentistry, Omaha, Nebraska 68178

Whereas prehearing spiral ganglion neurons (SGNs) rely faithfully on outputs from spontaneously active developing hair cells, the electrical phenotypes of posthearing neurons are shaped by distinct rapid and graded receptor potentials from hair cells. To date, technical difficulties in isolation of fragile posthearing neurons from the rigid bony labyrinth of the inner ear have hindered analyses of the electrical phenotype of SGNs. Therefore, we have recently developed new strategies to isolate posthearing mouse SGNs for functional analyses. Here, we describe the coarse and fine properties of Ca^{2+} currents, which sculpt the firing properties of posthearing SGNs. Murine SGNs express multiple Ca^{2+} channel currents to enable diverse functions. We have demonstrated that suppression of Ca^{2+} currents results in significant hyperpolarization of the resting membrane potential (rmp) of basal SGNs, suggesting that Ca^{2+} influx primes rmp for excitation. In contrast, removal of external Ca^{2+} has modest effects on rmp of apical SGNs. The blockade of Ca^{2+} currents with a mixture of specific blockers attenuates spontaneously active SGNs. Paradoxically, different subtypes of Ca^{2+} currents, such as R-type currents, may activate resting outward conductances since blockage of the current results in depolarization of rmp. In keeping with whole-cell current data, single-channel records revealed multiple diverse Ca^{2+} channels in SGNs. Additionally, there were differential expressions of distinct Ca^{2+} current densities in the apicobasal contour of the adult cochlea. This report provides invaluable insights into Ca^{2+}-dependent processes in adult SGNs.

Introduction

The spiral ganglion is the hub from which a set of (type 1) afferent neurons, which constitute ~95% of the total sensory cells (Morrison et al., 1975; Spoendlin, 1981), transmit precise and reliable information about the amplitude, duration, and frequency of acoustic waves from hair cells to the cochlear nucleus (CN). In addition to the primary role of faithfully encoding acoustic waves from hair cells to the CN, voltage-dependent changes in membrane excitability and corresponding intracellular Ca^{2+} (Ca_i^{2+}) fluctuations confer growth and survival of spiral ganglion neurons (SGNs) as well as other Ca^{2+}-dependent functions (Hegarty et al., 1997; Roehm et al., 2008). Moreover, a pragmatic role for SGN stimulation and Ca^{2+}-dependent neuronal survival is reflected in CN cell death following a blockade of SGN activity or cochlear ablation (Pasic and Rubel, 1989), which is underpinned by the utility of cochlear implants in hearing restoration (Leake et al., 1999).

Previous studies have demonstrated the presence of voltage-dependent Ca^{2+} currents in SGNs from guinea pigs to embryonic chickens and prehearing mice (Yamaguchi and Ohmori, 1990; Hisashi et al., 1995; Jiménez et al., 1997; Chen et al., 2011). Although these studies have provided a wealth of information concerning the histological expression of Ca^{2+} channels in prehearing neurons, and in one case the properties of L-type Ca^{2+} currents in guinea pig neurons (Hisashi et al., 1995), little is known about the properties of Ca^{2+} currents in posthearing SGNs, let alone their functions. Meanwhile, immunolocalization of Cav1.3, Cav2.1, and Cav2.3 subunits has been demonstrated in the chinchilla cochlea (Lopez et al., 2003). However, in previous reports, inner ear tissue was subjected to prolonged fixation and harsh decalcification processes, which may have compromised the antigenicity of the channel proteins (Lopez et al., 2003). An obstacle to understanding Ca^{2+} current functions and membrane properties of SGNs is the lack of recordings from posthearing adult neurons. Invariably, the prevailing physiological data on ionic currents in SGNs have been obtained from prehearing SGNs (Jiménez et al., 1997; Adamson et al., 2002b; Chen et al., 2011) because of technical constraints in isolating and/or recording from fragile neurons in the posthearing matured bony labyrinth of the inner ear (Adamson et al., 2002a; Jagger and Housley, 2002, 2003).

In this report we have demonstrated that adult murine SGNs rely on the contribution of Ca^{2+} influx through Ca^{2+} channels to control not only the resting membrane potentials, but also the

Received May 1, 2012; revised Sept. 14, 2012; accepted Sept. 17, 2012.

Author contributions: E.N.Y. designed research; P.L., C.-R.S., W.W., H.J.K., S.M.R.-S., and E.N.Y. performed research; H.S. and S.M.R.-S. contributed unpublished reagents/analytic tools; P.L., C.-R.S., W.W., H.S., and H.J.K. analyzed data; E.N.Y. wrote the paper.

This work was supported by grants to E.N.Y. from the National Institutes of Health (DC003826). P.L. was funded by the National Organization for Hearing Research. We thank members of our laboratory for comments on this manuscript.

Correspondence should be addressed to Ebenezer N. Yamoah, Program in Communication Science, Department of Anesthesiology and Pain Medicine, Center for Neuroscience, 1544 Newton Court Davis, CA 95618. E-mail: enyamoah@ucdavis.edu.

DOI:10.1523/JNEUROSCI.2097-12.2012

 0270-6474/12/3016314-17$15.00/0

profile and coding of action potentials. These effects are mediated by multiple Ca^{2+} channel currents. Ca^{2+} currents fitting into the classification of L-type, N-type, P/Q-type, R-type, and T-type currents were identified at the whole-cell and single-channel current levels. The corresponding subunits responsible for the assembly of functional channels were localized in the membrane. Finally, differences in current densities in the apicobasal axis of the adult cochlea may contribute toward the distinct electrical features of apical and basal SGNs. The data presented in this report sets the framework for detailed cellular mechanisms of Ca^{2+}-dependent signaling in posthearing SGNs.

Materials and Methods

Isolation of adult SGNs. The present investigation was performed in accordance with the guidelines of the Institutional Animal Care and Use Committee of the University of California, Davis. SGNs were isolated from the mouse inner ear using a combination of enzymatic and mechanical procedures (Wei et al., 2007). Adult male and female (3–4 months old) C57 mice were killed and the temporal bones were removed in a solution containing Minimum Essential Medium with HBSS (Invitrogen), 0.2 g/L kynurenic acid, 10 mM $MgCl_2$, 2% fetal bovine serum (FBS; v/v), and glucose (6 g/L). The central spiral ganglion tissue was dissected out and split into three equal segments—apical, middle, and basal—across the modiolar axis as described previously (Lv et al., 2010). Previous studies have used apical and basal segments of prehearing cochlea to identify extreme differences in membrane properties and ionic current expression in SGNs along the axis of the cochlea (Adamson et al., 2002b; Chen et al., 2011). Since the bony adult preparation was more susceptible to neuronal damage than the cartilaginous prehearing cochlea, we used the apical and basal thirds to ensure adequate viable neuronal yield for the experiments (Lv et al., 2010). Additionally, we pooled three 3–4-month-old mice into each SGN culture. A potential drawback in the present study is the paucity of sufficient neurons obtained when the cochlea was divided into more than three segments, as described for prehearing cochlea (Chen et al., 2011). Using the basal and apical thirds may produce heterogeneity of SGNs that may potentially mask any apparent distinctions between apical and basal neurons.

The apical and basal tissues were digested separately in an enzyme mixture containing collagenase type I (1 mg/ml) and DNase (1 mg/ml) at 37°C for 20 min. After a series of gentle triturations and centrifugation in 0.45 M sucrose, the cell pellets were reconstituted in 900 ml of culture media [Neuralbasal-A, supplemented with 2% B27 (v/v), L-glutamine 0.5 mM, penicillin 100 U/ml; Invitrogen], and filtered through a 40 μm cell strainer for cell culture and electrophysiological experiments. For adequate voltage-clamp and satisfactory electrophysiological experiments, we cultured SGNs for ~24–48 h to allow the detachment of Schwann cells from neuronal membrane surfaces. Additionally, by recording from neurons after ~24–48 h after dissociation, we avoided neurons with extensive neurite outgrowth to reduce space clamp problems. An advantage in recording from adult neurons is that neurite outgrowth was less pronounced compared with prehearing neurons. Nonetheless, to minimize space clamp artifacts, we targeted spherical neurons with reduced neurite outgrowth for voltage-clamp experiments (Bar-Yehuda and Korngreen, 2008). All electrophysiological experiments were performed at room temperature (21–22°C). Reagents were obtained from Sigma Aldrich unless otherwise specified.

Electrophysiology. Action potentials were amplified (100×), filtered (bandpass 2–10 kHz), and digitized at 5–500 kHz. Extracellular solution for most experiments contained the following (in mM): 145 NaCl, 6 KCl, 1 $MgCl_2$, 0–2 $CaCl_2$, 10 D-glucose, and 10 HEPES, pH 7.3. Alterations of Ca^{2+} were adjusted with Mg^{2+}. The Ca^{2+} concentrations in nominal solutions were measured with a Ca^{2+}-sensitive electrode as described previously (Yamoah et al., 1998). To suppress Ca^{2+} influx through Ca^{2+} channels, we reduced the external Ca^{2+} concentration further to ~10 nM using custom-written software (maxchelator.stanford.edu/CaMgATPEGTANIST.htm). For perforated patch experiments, the tips of the pipettes were filled with the internal solution containing the following (in mM): 150 KCl, 10 HEPES, 10 D-glucose, pH 7.3. The pipettes were front-filled with the internal solution and back-filled with the same solution containing 250 μg/ml amphotericin.

Using an Axopatch 200B amplifier (Molecular Devices), whole-cell and cell-attached single-channel voltage-clamp recordings of Ca^{2+}/Ba^{2+} currents were performed on adult SGNs. Current traces were amplified, filtered (bandpass 2 kHz), and digitized at 5–500 kHz using an analog-to-digital converter, Digidata 1200 (Molecular Devices), as described previously (Rodriguez-Contreras and Yamoah, 2001; Levic et al., 2007). Fire-polished electrodes (2–3 MΩ) were pulled from borosilicate glass. The electrodes contained the following (in mM): 70 CsCl, 70 *N*-methyl-D-glucamine chloride, 1 $MgCl_2$, 10 HEPES, 2–5 EGTA, 1 $CaCl_2$, 4 Cs_2ATP, pH 7.2, with CsOH. The bath solution was constantly perfused (2–3 ml/min) and contained the following (in mM): 120 cholineCl, 20 tetraethylammonium chloride (TEACl), 5 4-aminopyridine (4-AP), 0.02 linopirdine, 2 CsCl, 1.8–5 $CaCl_2$, 0.5–5 $MgCl_2$, 10 HEPES, 5 D-glucose, pH 7.40, with NaOH. In all cases when the Ca^{2+} concentration was altered, Mg^{2+} substitution was used to minimize membrane surface charge effects. Inward Ca^{2+} current traces were generated with depolarizing voltage steps from a holding potential of −90/−70 mV and stepped to varying positive potentials ($\Delta V = 2.5$–10 mV). The capacitative transients were used to estimate the capacitance of the cell as an indirect measure of cell size. The seal resistance was typically 10–15 GΩ. Currents were measured with capacitance compensation and series resistance compensation (>90%), filtered at 2 kHz using an eight-pole Bessel filter, and sampled at 5 kHz. Given that the maximum current recorded was <1 nA, the expected voltage error was <1.5 mV. The series resistance was monitored during the course of the experiments. The liquid junction potentials were measured and corrected. In addition to these standard requirements for acceptance of data, several basic criteria were set to ensure optimum quality of recordings and acceptance of data. The basic criteria set included: (1) initialing stable seals for at least 5 min before recordings; (2) eliminating cells with current traces that exhibit signs of voltage inhomogeneities; (3) removing cells with outward current contaminations; and (4) excluding cells with >20% change in the series resistance before and during recordings.

Whole-cell Ca^{2+} current amplitudes at varying test potentials were measured at the peak and steady-state levels using a peak and steady-state detection routine; the current magnitude was divided by the cell capacitance (pF) to generate the current density–voltage relationship. The stock solutions of all channel blockers and agonists were made either in double-distilled water or DMSO and stored at −20°C. The final concentration of DMSO in the recording bath solution was ~0.0001%. This concentration of DMSO had no effects on action potentials, nor did it alter Ca^{2+} current recordings (data not shown). The cell-attached configurations of the patch-clamp technique (Hamill et al., 1981) was used to record single Ca^{2+} channel currents from adult SGNs. Patch electrodes were pulled from borosilicate glass capillaries with a Flaming/Brown microelectrode puller (P97, Sutter Instrument), coated with Sylgard 184 (Dow-Corning) to within 100 μm from the tip, and fire-polished before use. Single-channel recordings of membrane patches were held at −90 or −70 mV, and stepped to different depolarizing test pulses at frequencies between 0.2 and 0.5 Hz. Current traces were amplified and filtered using an eight-pole Bessel filter at 2 kHz, and digitized at 10 kHz using custom-written software. Patch electrodes were filled with a Ba^{2+} solution (50 mM) containing (mM) 20 *N*-methyl-D-glucamine (NMG), 20 TEACl, 5 4-AP, and 5 HEPES, pH 7.4 [adjusted with tetraethylammonium hydroxide (TEAOH)]. The osmolarity of the patch-electrode solution was ~290 mosmol. Stock solutions of Bay K 8644 (10 mM) were made in DMSO, and a final concentration of 5 μM was used. The bath solution contained (in mM) the following: 80 KCl, 3 D-glucose, 20 TEACl, 0.5 $CaCl_2$, 5 4-AP, and 5 HEPES, pH 7., with TEAOH to shift the resting potential to ~0 mV (Rodríguez-Contreras and Yamoah, 2003). The Ca^{2+} channel blockers, nimodipine (L type), ω-conotoxin MVIIA (CTX; N type), ω-agatoxin IVA (ATX; P/Q type), ω-theraphotoxin-Hg1a, ω-TRTX-Hg1a (rSNX-482; R type) (Alomone Labs), and mibefradil (T type) channels were bath-applied for whole-cell and single-channel recordings. Additionally, for single-channel recordings, toxins were backfilled in the pipette solutions for cell-attached experiments. In all cases, liquid junction potentials

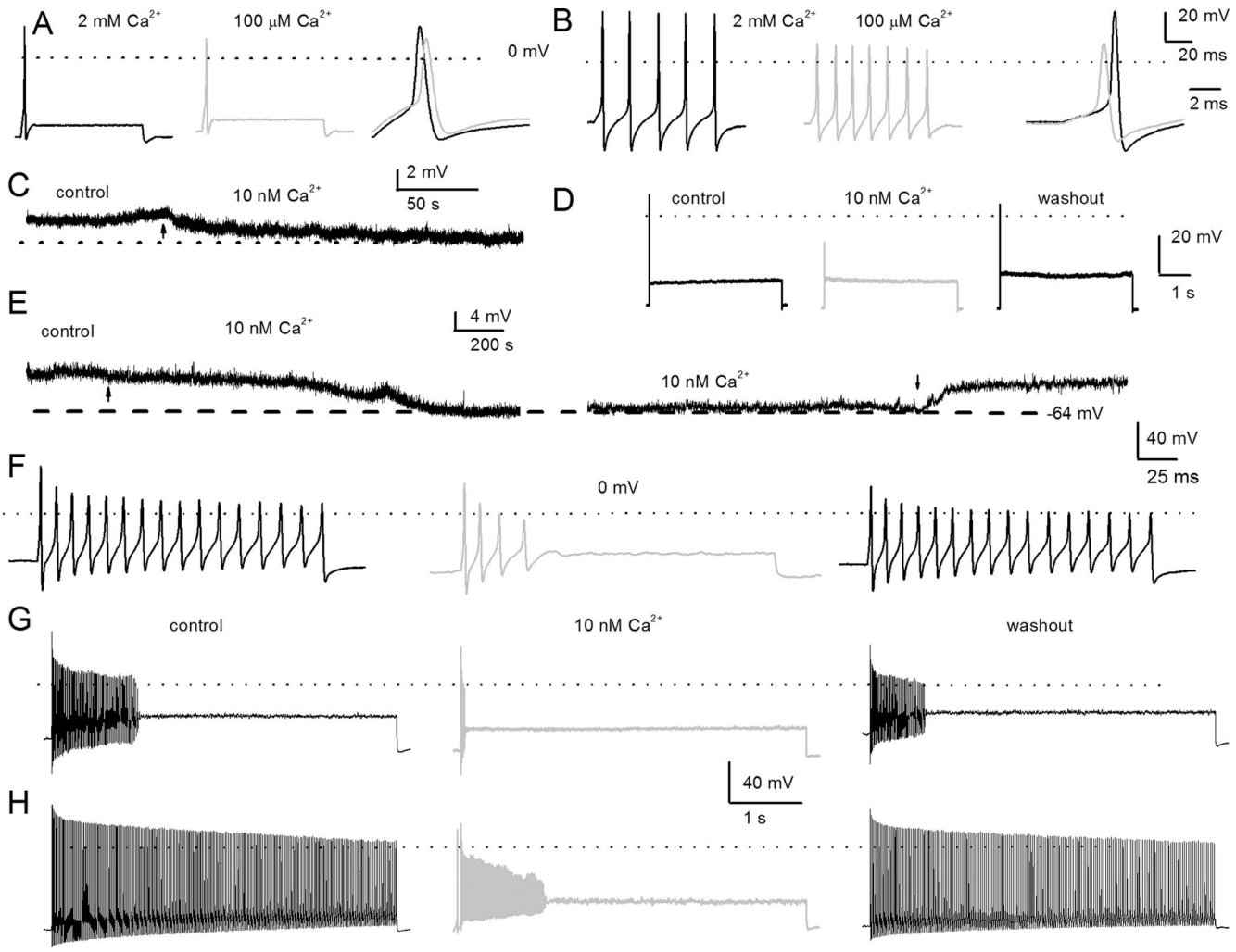

Figure 1. Effects of changes in external Ca^{2+} on action potentials in posthearing spiral ganglion neurons. ***A***, We used the perforated-patch configuration to evoke electrical activity from apical, rapidly adapting SGNs in 2 mM extracellular Ca^{2+} (left, black) and after (middle, light gray) bath perfusion of extracellular solution containing ~100 μM Ca^{2+}. The magnitude and duration of the injected current were 0.2 nA and 100 ms, respectively. On the right panel, we superimposed evoked action potentials recorded in 2 mM Ca^{2+} and 100 μM Ca^{2+} solution. The peaks of the action potentials were 28 ± 3 mV in 2 mM Ca^{2+}, and 10 ± 6 mV in 100 μM Ca^{2+} bath solutions ($n = 8$; $p < 0.05$), and the maximum right slopes were −99 ± 16 mV/ms in 2 mM Ca^{2+}, and −78 ± 4 mV/ms in 100 μM Ca^{2+} bath solution ($n = 8$; $p < 0.05$). ***B***, Evoked action potentials were elicited with a 0.05 nA current for ~100 ms from a basal, slowly adapting, SGN in a bath solution containing 2 mM Ca^{2+} (left) and after (middle) a bath perfusion of ~100 μM Ca^{2+}solution. The right panel shows a comparison of action potential profiles in the two treatment conditions. The dotted lines show 0 mV levels. The peaks of the action potentials were 37.0 ± 7 mV in 2 mM Ca^{2+}, and 16 ± 3 mV in 100 μM Ca^{2+} bath solutions ($n = 9$; $p < 0.05$), and the maximum right slopes were −149 ± 1 mV/ms in 2 mM Ca^{2+}, and −83 ± 15 mV/ms in 100 μM Ca^{2+} bath solution ($n = 9$; $p < 0.05$). ***C***, The characteristic rmp of a 3-month-old apical SGN. Reduction of external Ca^{2+} from 2 mM to ~10 nM produced modest hyperpolarization of the rmp. The summary data show that the rmp for apical neurons was, for control, −58 ± 6 mV and, for 10 nM Ca^{2+}, −61 ± 4 mV ($n = 9$; $p = 0.12$). The effect of reduced Ca^{2+} was reversible after washout with control solution. ***D***, Injection of 0.2 nA current produced single spikes in apical SGNs. ***E***, Exemplary current-clamp recordings from SGNs from the basal turn of the cochlea showed the rmp in control solutions and after application of 10 nM Ca^{2+} solution. The effects of 10 nM Ca^{2+} solution were reversible. Summary data from 15 basal SGNs show that the rmp in control solution was −55 ± 5 mV and in 10 nM Ca^{2+} solution was −64 ± 3 mV ($n = 15$; $p < 0.05$). ***F–H***, The spike frequency of adult basal SGNs was heterogenous. Data from the same neuron after injection of 0.2 nA current for ~200 ms (***F***) and ~5 s (***G***), respectively. In 10 nM external Ca^{2+}, the spike frequency plummeted by ~5-fold compared with control (control, 17 ± 7 Hz; 10 nM Ca^{2+}, 3 ± 2 Hz; $n = 9$; $p < 0.05$). Upon washout, the spike frequency was restored to 12 ± 7 Hz ($n = 9$; $p = 0.08$). ***H***, In slowly adapting SGNs that fire unabatedly after injecting 0.2 nA for 5 s, the spike frequency was reduced by ~4-fold after application of 10 nM Ca^{2+} solutions. From control to 10 nM Ca^{2+} solution, the spike frequency changed from 49 ± 10 Hz (control) to 12 ± 6 Hz (10 nM Ca^{2+}) ($n = 11$; $p < 0.05$). The firing frequency after washout was 39 ± 14 Hz ($n = 11$; $p = 0.11$).

were measured and corrected as described previously (Rodriguez-Contreras et al., 2002).

For single-channel recordings, leakage and capacitative transient currents were subtracted by fitting a smooth template to null traces. Leak-subtracted current recordings were idealized using a half-height criterion (Rodriguez-Contreras and Yamoah, 2001, 2008). Transitions between closed and open levels were determined by using a threshold-detection algorithm, which required that two data points exist above the half-mean amplitude of the single-unit opening. The computer-detected openings were confirmed by visual inspection, and sweeps with excessive noise were discarded. Amplitude histograms at a given test potential were generated and then fitted to a single Gaussian distribution using a Levenberg-Marquardt algorithm to obtain the mean and SD. At least four voltage steps and their corresponding single-channel currents were used to determine the unitary conductance. Single-channel current–voltage relations were fitted by linear least-square regression lines and single-channel conductances obtained from the slope of the regression lines. Idealized records were used to construct ensemble-averaged currents, open probability, and histograms for the distributions of open and closed intervals. Curve fits and data analyses were performed using Origin software (MicroCal). Where appropriate, we presented data in the form of means ± SD. The mean values (n) listed represent data for each experimental group. Significant differences between groups were tested using paired/unpaired Student's t test.

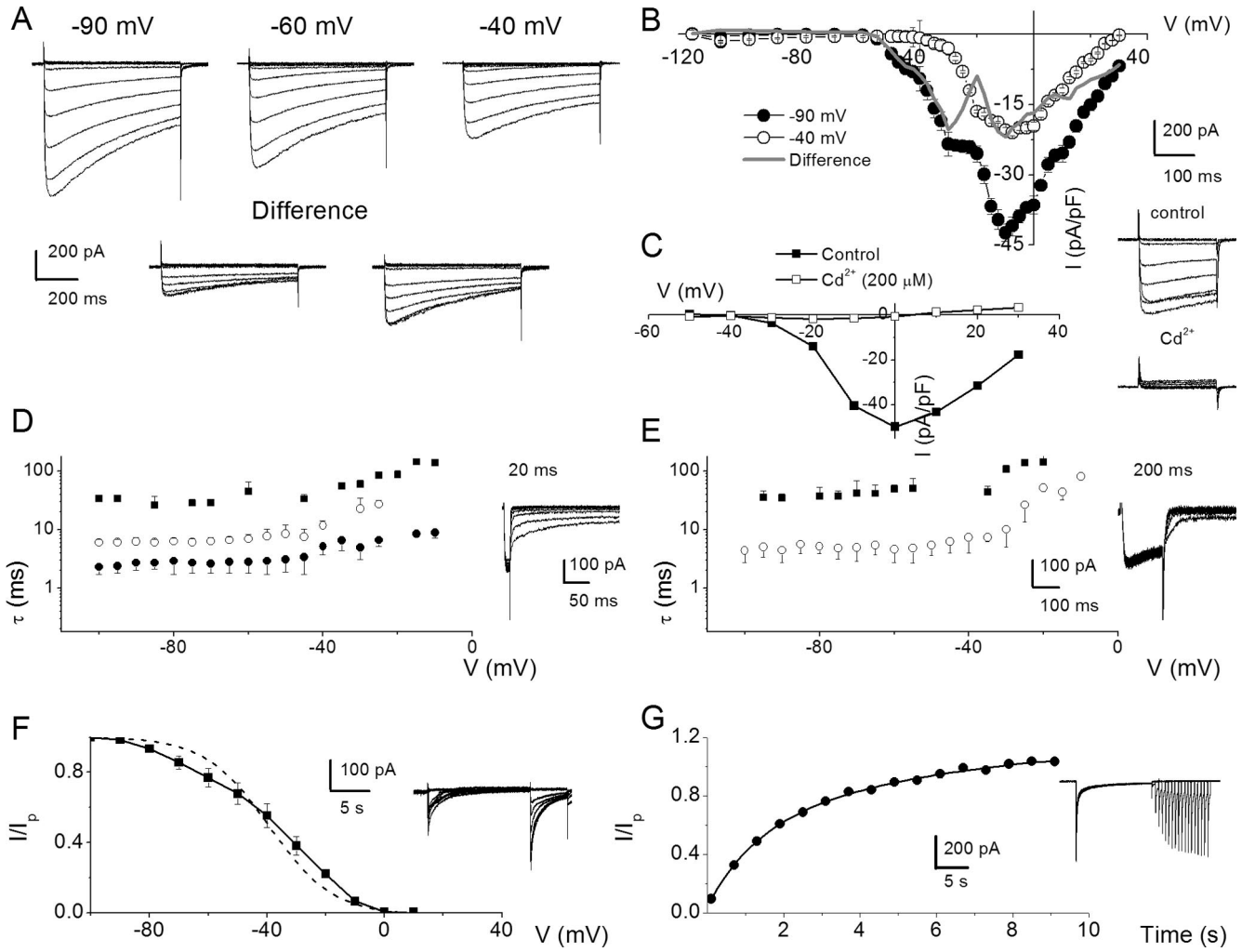

Figure 2. Whole-cell Ca^{2+} currents in SGNs may contain several components. ***A***, A family of membrane Ca^{2+} current traces recorded from SGNs using 5 mM external Ca^{2+}. Inward Ca^{2+} currents were generated using depolarizing test voltages from −120 to 30 mV in 2.5–10 mV increments from a holding voltage of −90 mV. Current traces recorded from the same neuron from a holding voltage of −60 and −40 mV. The difference between current traces recorded at −90 and −60 mV (left, inset) and −90 and −40 mV (right, inset) holding voltages. ***B***, Summary of the corresponding I–V relations for recordings at −90 (●) and −40 (○) mV holding voltages. Gray line shows the difference between currents at −90 and −40 mV. Data were summarized from $n = 15$. ***C***, A family of control current traces generated from a holding voltage of −70 mV (right, inset). After application of Cd^{2+} (200 μM), the whole-cell Ca^{2+} current was blocked (inset). The corresponding I–V relations are shown (control, ■; Cd^{2+}, □). ***D***, SGNs were held at −80 mV and Ca^{2+} currents were elicited for 20 ms to 10 mV. At the end of the prepulse, the membrane voltage was polarized to different test voltages in 5 mV increments (between −100 and −5 mV), and the kinetics of the tail currents were examined. ***E***, A similar protocol was applied using a 200 ms prepulse. The current traces are shown as insets. Summary data of the relations between the time constant of deactivation (■,●,○) and test voltages using 20 (***D***) and 200 ms (***E***) prepulses ($n = 10$). Invariably, multiple deactivation time constants were documented using shorter prepulse voltages. Three time constants were derived using 20 ms prepulse. In contrast, two time constants best fitted the deactivation kinetics using 200 ms prepulse. ***F***, Exemplary current traces elicited to generate steady-state inactivation curves depicted in inset. The neuron was held at −70 mV and stepped to conditioning voltages varying from −100 to 40 mV for ~15 s, followed by a test voltage at 10 mV. The current was normalized against the noninactivating component evoked at the test voltage. The dotted curve represents a first-order Boltzmann function fit. However, the data were best fitted with a second-order Boltzmann function (solid line). The half-inactivation voltages ($V_{½–1}$, mV) were −65 ± 8 (at ~35% contribution) and ($V_{½–2}$) −32 ± 3 (at ~65% contribution) ($n = 9$) and the maximum slope factors (k, in mV) were 9.0 ± 1 and 10 ± 2 ($n = 9$). ***G***, Neurons were held at −80 mV and stepped to conditioning prepulse (10 mV) to make a transition from activation to inactivation. Subsequently, test pulses at varying time intervals were applied. The traces shown in inset are a family of currents obtained after applying a set of pulses as described. The currents elicited at the test pulse at specific times after the conditioning prepulse were normalized against conditioning pulse-evoked current and plotted against time. At least two time constants (τ) of recovery from inactivation were obtained: $\tau 1$, 1.3 ± 0.2 s; $\tau 2$, 7.2 ± 1.6 s; $n = 11$.

Immunocytochemistry. SGNs were isolated from the mouse inner ear and cultured for 48 h as described previously (Lv et al., 2010). Neurons were fixed for 30 min with 2% paraformaldehyde, washed, and then permeabilized in 0.5% Triton X-100 for 5 min. The samples were incubated for 1 h in a blocking solution containing PBS and 1% horse serum, followed by 3–5 h incubation with Ca^{2+} channel antibodies against Cav1.3, residues 859–875; Cav2.1, residues 865–881; Cav2.2, residues 851–867 (Alomone Labs); and Cav2.3, residues 2200-C terminal (Abcam), at 1:100–1:500 dilutions. To identify neurons, samples were counter-stained with antibody against the neuronal marker TUJ1 as described previously (Wei et al., 2008). Cells were then incubated with appropriate secondary antibodies for 2 h, washed, mounted using antifade mounting medium, and viewed with a Zeiss LSM 510 confocal microscope.

For histological cryosection experiments, sedated [Avertin (2,2,2,tribromoethanol); 300 μg/gm body weight, i.p.] mice were transcardially perfused with 10 ml of PBS followed by 10 ml of 4% paraformaldehyde in 0.1 M PBS. The temporal bones were removed, and the cochleae were perfused via the oval and round windows. The temporal bones were then immersed in fixative for 60 min. After fixation, the cochleae were decalcified (120 mM EDTA, pH 7.0; 24 h; ~21°C). Cochleae were processed sequentially with 10 and 30% sucrose at 4°C overnight then embedded in OTC for cryosection. Sections were washed in PBS, permeabilized in 0.1% Triton X-100 for 25 min, and then incubated for 30 min in a blocking solution containing 1% bovine serum albumin and 1% goat serum. The 10 μm sections were incubated with primary antibody overnight at 4°C. The rinsed sections were then incubated (2 h; 4°C) in fluo-

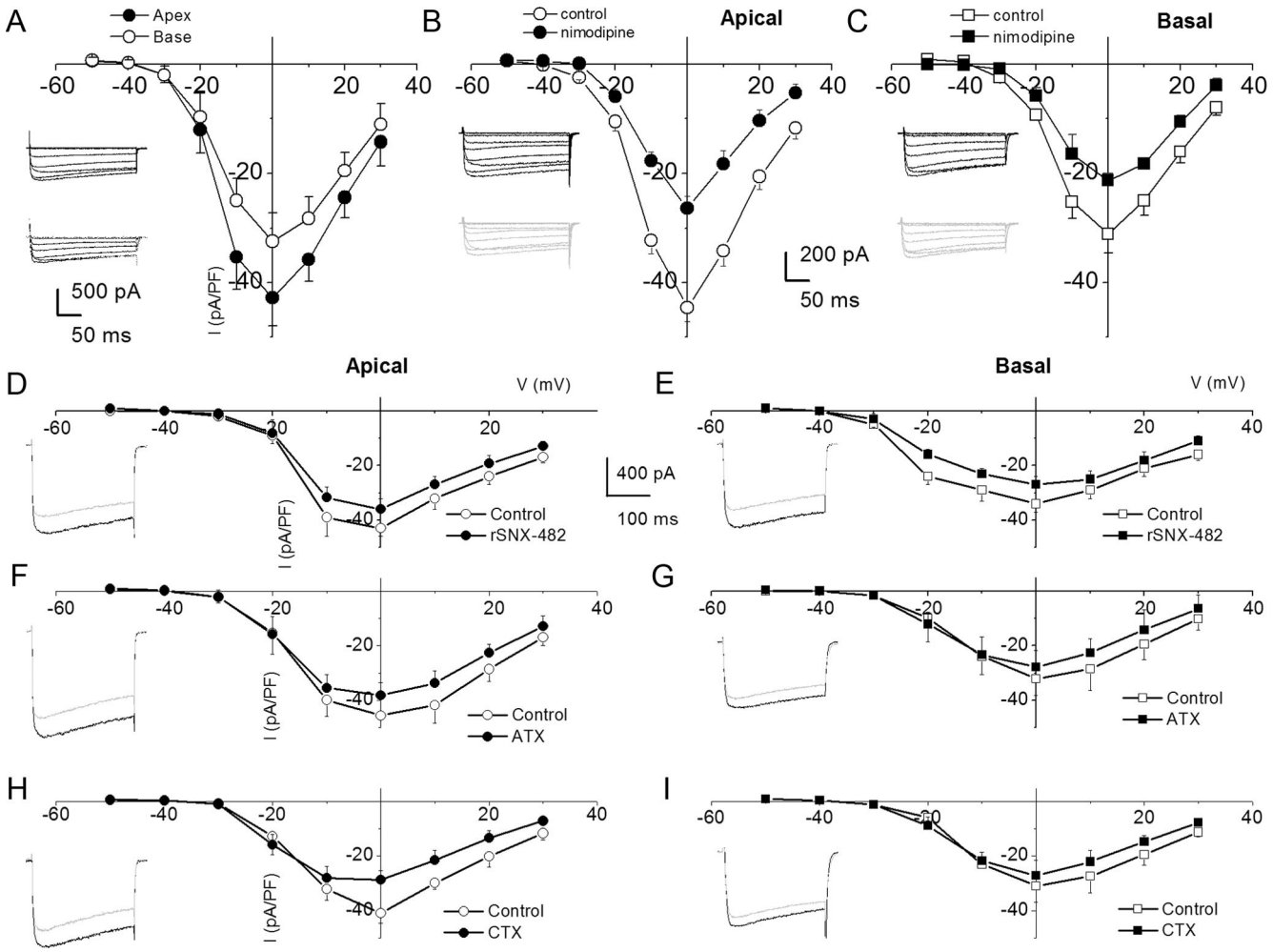

Figure 3. Characteristics of Ca^{2+} currents in 3-month-old SGNs from apical and basal turns of the cochlea, and the effects of Ca^{2+} current blockers. ***A***, Family of inward Ca^{2+} currents from apical SGN elicited from a holding potential of −70 mV to step potentials from −50 to 30 mV in 10 mV increments (left, inset). A similar voltage pulse protocol was applied to generate Ca^{2+} current traces from basal SGNs (right, inset). Peak Ca^{2+} current density–voltage relations for apical (●) and basal (○) SGNs. At voltages (−10–10 mV), there were significant differences between apical and basal Ca^{2+} current densities (*$p < 0.05$; $n = 17$). ***B***, The DHP antagonist, nimodipine, blocks a component of whole-cell Ca^{2+} currents in SGNs. Current traces recorded from neurons isolated from apical [top, inset (control); bottom, inset (nimodipine)] segments of the cochlea. Perfusion of external solution containing 10 μM nimodipine resulted in a reduction of the Ca^{2+} currents. The corresponding current density–voltage relations for apical (***B***) and basal (***C***) SGNs ($n = 9$). The control data are illustrated with black lines and symbols and the residual current after nimodipine block is shown in blue lines and symbols. ***D–I***, The current density–voltage relations were generated before (black lines and symbols) and after (blue lines and symbols) application of Ca^{2+} current blockers: rSNX-482 for R-type currents (***D***, ***E***); ATX for P/Q-type currents (***F***, ***G***); and CTX for N-type currents (***H***, ***I***). ***D***, ***E***, Current density–voltage relations for control (black) and the remaining current density after application of toxins (blue) for apical (***D***) and basal (***E***) SGNs ($n = 6$). The insets in the left panels of the plots are representative current traces recorded from a holding voltage of −70 mV to a step voltage of 0 mV. ***F***, ***G***, Similar data obtained upon recording control Ca^{2+} currents and after application of the P/Q-type Ca^{2+} current blocker, 1 μM ATX. ***H***, ***I***, Summary data of the effects of the N-type Ca^{2+} channel blocker on apical versus basal neurons. Table 1 illustrates the summary data for the effects of Ca^{2+} channel blockers on whole-cell Ca^{2+} currents.

Table 1. Percentage of Ca^{2+} current blocked by different blockers at 0 mV step voltage

	L type	P/Q type	N type	R type	Total
Blocker	Nimodipine	ATX	CTX	rSNX-482	
Concentration	10 μM	1 μM	1 μM	200 nM	
Apex	41.0 ± 4.5%	17.2 ± 2.7%	22.6 ± 4.3%	15.9 ± 5.7%	81.6 ± 7.8%
Base	31.2 ± 2.9%*	11.5 ± 5.9%	12.6 ± 2.3%*	19.5 ± 5.1%	71.1 ± 6.2%

*$p < 0.05$ (apex vs base) ($n = 6$).

rescent dye-conjugated secondary antibody. Images were captured with a Zeiss LSM 510 confocal microscope.

Results

Effects of Ca^{2+} on the membrane properties of adult SGNs

Previous studies have shown that, in prehearing spiral ganglion, almost all neurons in the base adapt rapidly, while neurons in the apex adapt at varying rates (Adamson et al., 2002a,b). In posthearing adult spiral ganglia, neural responses were invariably heterogeneous, ranging from spontaneously active to evoked rapidly adapting neurons in both basal and apical aspects of the cochlea. Thus, we classified neurons not only by their location in the cochlea but also by their evoked firing frequency as rapidly adapting (<5 Hz), moderately adapting (6–20 Hz), and slowly adapting (>20 Hz) neurons using 0.2 nA current injection. To determine the coarse features of Ca^{2+} currents on membrane properties of SGNs, classical ion substitution experiments were performed by examining evoked action potentials in rapidly (from apical third) and slowly (from basal third) adapting neurons in the presence of bath solutions containing Ca^{2+} (2 mM) and nominal Ca^{2+} (~100 μM). To minimize changes in membrane potential as a result of surface charge effects, Ca^{2+} was replaced with equal concentrations of Mg^{2+}. Reduction of Ca^{2+} concentration had three noticeable effects on the membrane

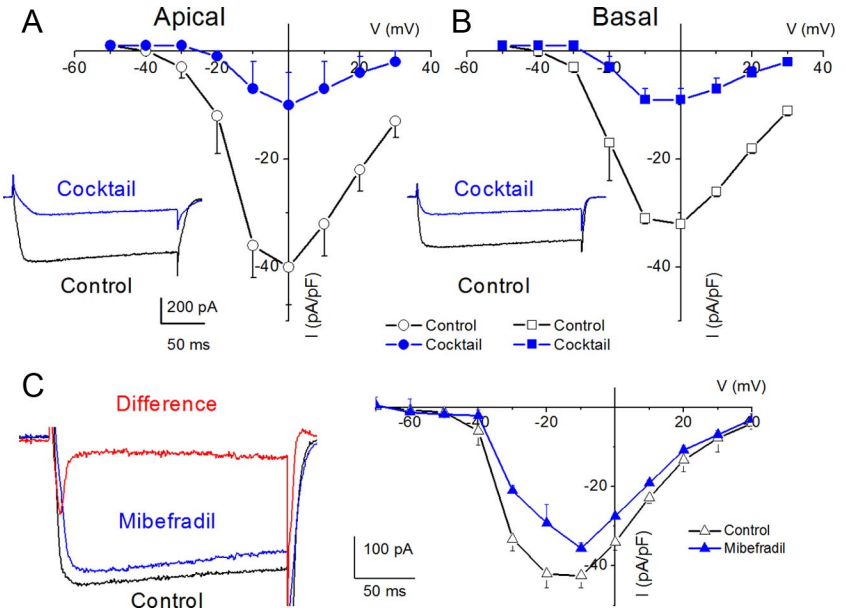

Figure 4. Whole-cell Ca^{2+} currents in SGNs resistant to a mixture of L-type, N-type, P/Q-type, and R-type current blockers and mibefradil-sensitive currents. A mixture of 10 μM nimodipine, 1 μM ATX, 1 μM CTX, and 200 nM rSNX-482 was used. ***A***, Current traces recorded using a holding voltage of −70 to a step voltage of 0 mV in apical neurons (control current trace, black; after application of blocker mixture, blue). **B,** Similar data obtained from basal neurons as described by ***A***. The corresponding current density–voltage relations for apical (***A***) and basal (***B***) neurons ($n = 7$). The mixture blocked 81.6 ± 7.8% ($n = 7$) of the total Ca^{2+} currents in apical neurons. Meanwhile, 71.1 ± 6.2% ($n = 7$) of the total Ca^{2+} currents were blocked in basal neurons. ***C***, Ca^{2+} current traces from a basal SGN held at a holding potential of −90 mV and stepped to −10 mV. The control trace (black) and the residual current after application of 5 μM mibefradil (blue) are shown. The difference current or the mibefradil-sensitive current shows a transient profile, consistent with T-type Ca^{2+} currents (red). The corresponding current–voltage relations are shown from data from four basal SGNs.

properties of SGNs. First, the reduction of external Ca^{2+} mediated a small but marked membrane hyperpolarization that appeared to be more pronounced in slowly adapting neurons than in rapidly adapting neurons (Fig. 1*A,B*). Second, as expected from the contribution of Ca^{2+} currents toward the upstroke phase of action potentials, the 0 mV overshoot was increased in the presence of external Ca^{2+}. In the presence of 2 mM Ca^{2+}, the repolarization phase of the action potentials in slowly adapting neurons was more prominent than with nominal Ca^{2+} (Fig. 1, legend). The effects of increased external Ca^{2+} may result from the Ca^{2+} dependence of activation of K^+ and/or Cl^- currents in SGNs (Adamson et al., 2002b). To further suppress inward Ca^{2+} currents, an external solution with a calculated Ca_i^{2+} of ~10 nM was used (Fig. 1*C–I*). As amplified in Figure 1*C*, a switch from control to 10 nM Ca^{2+} solution resulted in modest hyperpolarization of the resting membrane potential (rmp) of the rapidly adapting apical SGN (rmp: control, −58 ± 6 mV; 10 nM Ca^{2+}, −61 ± 4 mV; $n = 9$; $p = 0.12$). The effects of 10 nM external Ca^{2+} on action potential profiles were reversible (Fig. 1). In contrast to rapidly adapting neurons, 10 nM external Ca^{2+} solution produced significant hyperpolarization of the rmp (Fig. 1*E*) of the slowly adapting basal neuron. The rmp in the control solution was −55 ± 5 mV; in the 10 nM Ca^{2+} solution, rmp was −64 ± 3 mV ($n = 15$; $p < 0.05$). Figure 1*F–H* shows reversible effects of the 10 nM Ca^{2+} solution on the firing of two classes of nonrapidly adapting basal neurons: moderately (Fig. 1*F–H*) and slowly adapting neurons (Fig. 1*H*). Using 0.2 nA current injection for 5 s, moderately adapting basal SGNs in the control solution yielded a mean firing frequency of 17 ± 7 Hz ($n = 9$), which plummeted to 3 ± 2 Hz ($n = 9$; $p < 0.05$) after application of the 10 nM Ca^{2+} solution. Upon washout, the control firing pattern was restored to 12 ± 7 Hz ($n = 9$; $p = 0.08$). Meanwhile, in a slowly adapting basal SGN, removal of Ca^{2+} currents with the 10 nM Ca^{2+} solution reduced the mean firing frequency by ~4-fold, from 49 ± 10 Hz to 12 ± 6 Hz ($n = 11$; $p < 0.05$). The effects of the 10 nM Ca^{2+} solution were reversed after a washout with control solutions, recovering to 39 ± 14 Hz ($n = 11$; $p = 0.11$). Whereas suppression of Ca^{2+} currents and the ensuing diverse alterations of membrane potential changes in SGNs may result from a single class of Ca^{2+} channel currents, it is equally likely that SGNs employ multiple channels to confer Ca^{2+}-dependent functions. Exhaustive cellular mechanisms of Ca^{2+}-mediated function can be gauged by understanding the transport features of Ca^{2+} channel currents.

Evidence for multiple Ca^{2+} currents in adult SGNs

To examine Ca^{2+} channel currents in SGNs, we suppressed outward K^+ currents with external TEA, 4-AP, linopirdine, internal Cs^+, and NMG^+ in a manner similar to previous analyses of Ca^{2+} current in hair cells (Rodriguez-Contreras and Yamoah, 2001, 2003; Adamson et al., 2002b). Additionally, we curbed contamination of inward Ca^{2+} currents by Na^+ currents by substituting external Na^+ with choline. The resulting exemplary current traces recorded from a holding voltage of −90 mV and voltage steps ranging from −120 to 30 mV with ΔV of 10 mV are shown in Figure 2*A* (for greater clarity, not all current traces were plotted). Upon shifting the holding voltage to −60 and −40 mV (Fig. 2*A*), the magnitudes of the Ca^{2+} current were visibly reduced, and the profiles of the time course of inactivation were altered as well. The difference–current traces between traces elicited from a holding voltage of −90, −60, and −40 mV (Fig. 2*A*) are in accordance with the possibility that membrane hyperpolarization relieves components or different subtypes of Ca^{2+} currents from their inactivated states. To further determine whether the apparent differences in the voltage dependence of the seemingly different subtypes of Ca^{2+} currents can be revealed in the current–voltage relation, we used small voltage steps (ΔV = 2.5 mV) to activate whole-cell Ca^{2+} currents, and the corresponding current density–voltage (I–V) curves are plotted as shown in Figure 2*B*. Using a holding potential of −90 mV, the peak current density was observed at ~−5 mV. The "shoulder" at −35 to −20 mV may reflect the peak activation of distinct Ca^{2+} currents with low-voltage activation properties. Upon holding SGNs at −40 mV, the "shoulder" current was abolished (Fig. 2*B*) and the "difference" I–V relations suggested the possibility that SGNs express more than one distinct Ca^{2+} current subtype. Moreover, to ensure that we were indeed recording Ca^{2+} currents, their sensitivity to Cd^{2+}, a nonspecific Ca^{2+} current blocker, was tested as demonstrated in Figure 2*C*. Although the access resistances of our recording conditions were nominal (see Materials and Methods), kinks in the I–V relations can be introduced by voltage errors (Yamoah and Crow, 1994; Bar-Yehuda and Korngreen, 2008), so we reduced the magnitude of the current by decreasing the external Ca^{2+} from 5 to 2 mM (3 mM Mg^{2+}

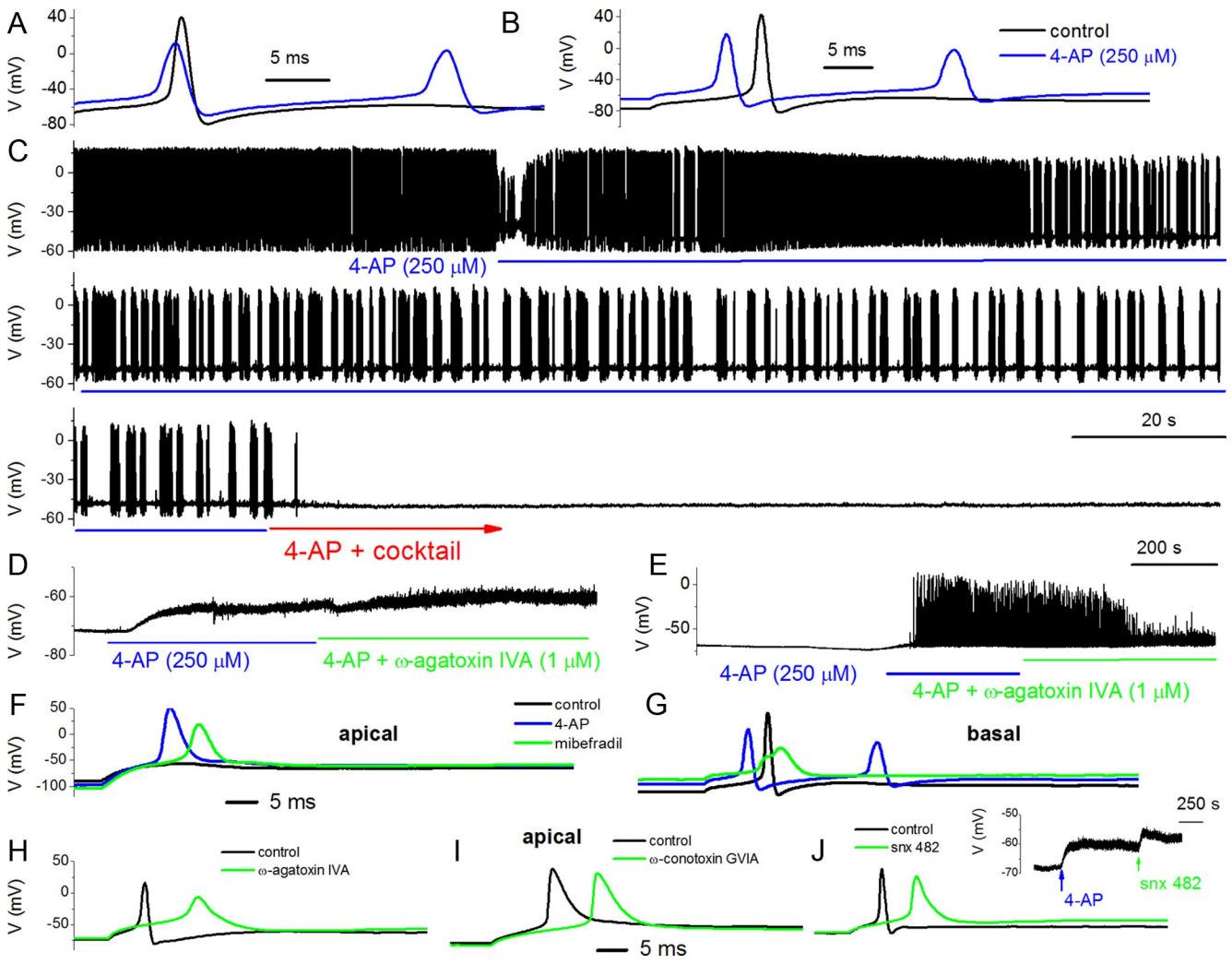

Figure 5. Effects of 4-AP and Ca^{2+} current blockers on membrane properties of adult SGNs. To enhance and resolve the effects of Ca^{2+} current blockers on action potentials in SGNs, we used 4-AP (250 μM) to broaden the action potentials. ***A***, Evoked action potentials (0.2 nA current) recorded from a 3-month-old basal SGN, before and after application of bath solution containing 250 μM 4-AP. ***B***, Rebound action potentials following injection of negative current (−0.5 nA). ***C***, In spontaneously active SGNs, 4-AP altered the firing pattern. Upon application of bath solution containing 4-AP and a mixture of Ca^{2+} current blockers (10 μM nimodipine for L-type currents, 1 μM ATX for P/Q-type currents, 1 μM CTX for N-type currents, 200 nM rSNX-482 for R-type currents, and 5 μM mibefradil for T-type currents), spontaneous activity was attenuated. ***D***, In addition to altering the shape and firing patterns of action potentials, 250 μM 4-AP was sufficient to produce substantial depolarization of SGNs (rmp for control, -65 ± 9 mV; after application of 4-AP, -61 ± 7 mV; $n = 8$). Blockade of P/Q-type Ca^{2+} currents with 1 μM ATX resulted in small but consistent depolarization of the rmp (controls, -64 ± 8 mV; after ATX, -57 ± 2 mV; $n = 8$). ***E***, In 6 of 10 SGNs, 4-AP-induced depolarization triggered spontaneous activity. Suppression of P/Q-type Ca^{2+} currents reduced the spike amplitude and frequency (5 of 6 SGNs). ***F***, Adult apical SGNs were injected with −0.5 nA, and slight rebound depolarization followed (black trace). Upon application of 250 μM 4-AP solution, injection of −0.5 nA sufficed to elicit rebound action potential (red). Green trace shows resulting action potential after application of bath solution containing 250 μM 4-AP and 5 μM mibefradil. ***G***, Similar but not identical data obtained from age-matched basal SGNs. ***H***, The resulting effects of blockade of P/Q-type current (control, black; after 4-AP and toxin, green traces) in apical SGNs. The 4-AP-mediated traces were omitted for clarity but see Table 2. ***I***, ***J***, Changes in action potential properties following inhibition of N-type and R-type Ca^{2+} currents, respectively. Shown in the inset is the effect of 4-AP and the R-type channel blocker on the rmp. Table 2 outlines the summary data from both apical and basal SGNs.

was substituted for Ca^{2+}) to evaluate the kinetics of the tail currents using short (20 ms) and long (200 ms) prepulses. Figure 2*D*,*E* shows that the tail currents elicited with 20 ms prepulses were fitted with multiple time constants (τs: 3 τs) consistent with currents generated from multiple Ca^{2+} channel subtypes. Moreover, upon application of 200 ms duration prepulses, the number of τs was invariably reduced (~2 τs; Fig. 2*E*), raising the possibility that the duration of the prepulse was sufficient to cause at least one subpopulation of Ca^{2+} channel currents to transition into nonconducting states. Analyses of the steady-state inactivation and the kinetics of recovery from inactivation all converged toward the likelihood that SGNs employ more than one Ca^{2+} channel subtype to confer Ca^{2+} influx (Fig. 2*F*,*G*).

Ca^{2+} currents in apical versus basal SGNs

The membrane conductances in SGNs across the cochlear axis are heterogeneous, yielding at least two distinct neurons: rapidly and slowly adapting neurons in prehearing ganglia (Adamson et al., 2002b). As demonstrated in Figure 1 and later in Figure 5, the diversity of the firing patterns of adult SGNs abound, ranging from spontaneously active to quiescent and rapidly adapting spike-evoked neurons. An intriguing and testable hypothesis is to predict that differential expression of Ca^{2+} currents in SGNs contributes toward diverse membrane properties. We examined Ca^{2+} current densities in apical one-third versus basal one-third of SGNs in the cochlea. Figure 3*A* shows comparisons of the current densities between apical and basal neurons. The magni-

Table 2. Effects of Ca^{2+} current blockers on action potentials

	Apex				Base			
Blocker	Number of cells	Latency (ms)	Amplitude (mV)	Width (ms)	Number of cells	Latency (ms)	Amplitude (mV)	Width (ms)
Mibefradil								
Control	7	3.2±1.4	93 ± 6	1.8 ± 0.4	6	8.4 ± 1.4	111 ± 10	9.2 ± 1.4
4-AP		3.0 ± 0.7	54 ± 11	3.8 ± 0.5		6.5 ± 0.7	78 ± 12*	11.6 ± 1.5
4-AP + mibefradil		3.5 ± 1.1	39 ± 9**	5.2 ± 0.9*		13.5 ± 2.6*	46 ± 15**	18.5 ± 1.8**
rSNX								
Control	8	4.1 ± 1.2	94 ± 8	1.9 ± 0.4	8	9.3 ± 0.9	107 ± 12	8.8 ± 1.6
4-AP		3.9 ± 1.5	71 ± 5	3.6 ± 0.3		6.7 ± 1.1	81 ± 9	10.2 ± 0.5
4-AP + rSNX		7.0 ± 2.0*	67 ± 10*	6.2 ± 0.3**		3.4 ± 0.4*	68 ± 16**	16 ± 1.4*
ATX								
Control	6	4.4 ± 1.6	105 ± 13	1.8 ± 0.6	5	9.5 ± 1.8	110 ± 12	8.6 ± 1.4
4-AP		3.9 ± 1.1	78 ± 12	2.9 ± 0.5		9.9 ± 2.3	86 ± 16	10.4 ± 1.6
4-AP + ATX		9.1 ± 2.3*	43 ± 10**	10 ± 1.5**		5.1 ± 0.5*	57 ± 14**	18.9 ± 2.2**
CTX								
Control	7	3.7 ± 1.3	97 ± 7	2.0 ± 0.3	7	8.2 ± 1.3	105 ± 15	7.9 ± 1.5
4-AP		3.2 ± 1.1	82 ± 16	3.2 ± 1.4		7.1 ± 1.5	89 ± 16	9.1 ± 2.1
4-AP + CTX		7.4 ± 1.3*	78 ± 20	4.1 ± 1.5		11.8 ± 0.5*	85 ± 20	12 ± 4.4
Nimodipine								
Control	8	4.0 ± 1.6	101 ± 14	1.7 ± 0.5	9	7.9 ± 1.8	121 ± 26	10 ± 1.3
4-AP		3.9 ± 1.4	89 ± 12	3.4 ± 0.6		7.2 ± 2.1	80 ± 13	13 ± 0.8
4-AP + nimodipine		6.8 ± 0.5*	71 ± 5*	8.1 ± 0.7*		3.1 ± 1.1*	51 ± 7*	19 ± 1.7*

*$p < 0.05$; **$p < 0.01$.

tude of Ca^{2+} currents in apical neurons was significantly larger than in basal neurons. Moreover, the coarse features of whole-cell Ca^{2+} currents may mask other subtle differences that may occur between apical and basal neurons. Thus, we examined the pharmacology of Ca^{2+} currents in apical and basal neurons (Fig. 3*B–I*).

Pharmacology of Ca^{2+} currents in SGNs supports the existence of multiple currents

After perfusion with bath solution containing 10 μM nifedipine, there was a significant reduction of whole-cell Ca^{2+} currents (data not shown). To cross-check whether the observed effect on the current was dihydropyridine (DHP)-specific, we examined the effects of Bay K 8644, the DHP agonist. Consistent with the actions of DHPs on L-type currents, Bay K 8644 induced a leftward shift in the activation voltage of the Ca^{2+} current by ~15 mV (data not shown). Neuronal and auditory hair cells express L-type Ca^{2+} currents activated at relatively higher negative voltages than their cardiac counterparts (Lewis and Hudspeth, 1983; Pérez-García et al., 1995; Platzer et al., 2000; Marcotti et al., 2003; Michna et al., 2003; Schnee and Ricci, 2003; Levic et al., 2007; Zampini et al., 2010). The shift in I–V relation after application of the DHP agonist suggested that the DHP-sensitive current in SGNs belonged to the neuronal L-type current. Because neuronal $Ca_v1.3$ channel currents are less sensitive to the DHP antagonists (Xu and Lipscombe, 2001; Helton et al., 2005), and since nimodipine is a more potent blocker (Bean, 1984; Rodriguez-Contreras and Yamoah, 2001), we switched to nimodipine. Figure 3*B*,*C* shows representative current traces (insets) and the summary data of the effects of the DHP antagonist on apical versus basal SGNs (Table 1). The pharmacology of the DHP-resistant currents was tested further using other known specific organic Ca^{2+} current blockers. Using ATX for P/Q-type Ca^{2+} currents, CTX for N-type Ca^{2+} currents, rSNX-482 for R-type Ca^{2+} currents, mibefradil for T-type Ca^{2+} currents, and a mixture of blockers, we demonstrated that SGNs expressed these multiple current subtypes in apical and basal neurons (Figs. 3, 4). The residual current remaining after application of the combined blocker solution may consist of transient, T-type Ca^{2+} currents. In five cells (3 basal and 2 apical) in which the recording conditions were in accordance with the criteria for acceptable data (see Materials and Methods), a mibefradil-sensitive transient current ensued when cells were held at a holding potential of −90 mV and stepped to depolarizing voltages (Fig. 4*C*, red trace, mibefradil-sensitive current). The summary data are presented in the current–voltage relationship, which represents data from three basal SGNs.

Analyses of the contribution of Ca^{2+} currents on membrane properties

We examined the effects of Ca^{2+} currents on membrane potentials first by producing moderate action potential broadening using external 4-AP (250 μM). The action potential width of apical neurons was 1.9 ± 0.3 ms ($n = 56$) and, after application of 250 μM 4-AP, the action potential width increased to 4.2 ± 0.6 ms (Fig. 5*A*,*B*). Moreover, AP width of basal neurons was 3.2 ± 0.4 ms ($n = 16$) and, after application of 250 μM 4-AP, the action potential width increased to 4.6 ± 0.7 ms. In addition to changes in spike width, 4-AP altered the firing pattern of spontaneously active neurons (Fig. 5*C*). A mixture of Ca^{2+} current blockers, namely nimodipine for L-type currents, ATX for P/Q-type currents, CTX for N-type currents, rSNX-482 for R-type currents, and mibefradil for T-type currents, rendered spontaneously active neurons quiescent (Fig. 5*C*). Second, we assessed the effects of individual Ca^{2+} current blockers. Figure 5*D* shows the effect of 4-AP and ATX on the rmp. Suppression of the P/Q-type Ca^{2+} current resulted in small but consistent depolarization of the rmp. In neurons in which 4-AP-mediated spontaneous action potentials can be observed, application of ATX decreased spike amplitude and attenuated spontaneous action potentials with time (Fig. 5*E*). For individual spikes, suppression of P/Q-type current produced an increased action potential latency, duration, and increased spike width, as well as a suppression of membrane afterhyperpolarization (AHP) (Fig. 5*H*, Table 2). The findings on the contribution of P/Q-type currents were similar but not identical to the role of R-type currents, as illustrated in Figure 5*J* and summarized in Table 2. The mibefradil-sensitive currents contribute toward the upstroke phase, amplitude, and latency of

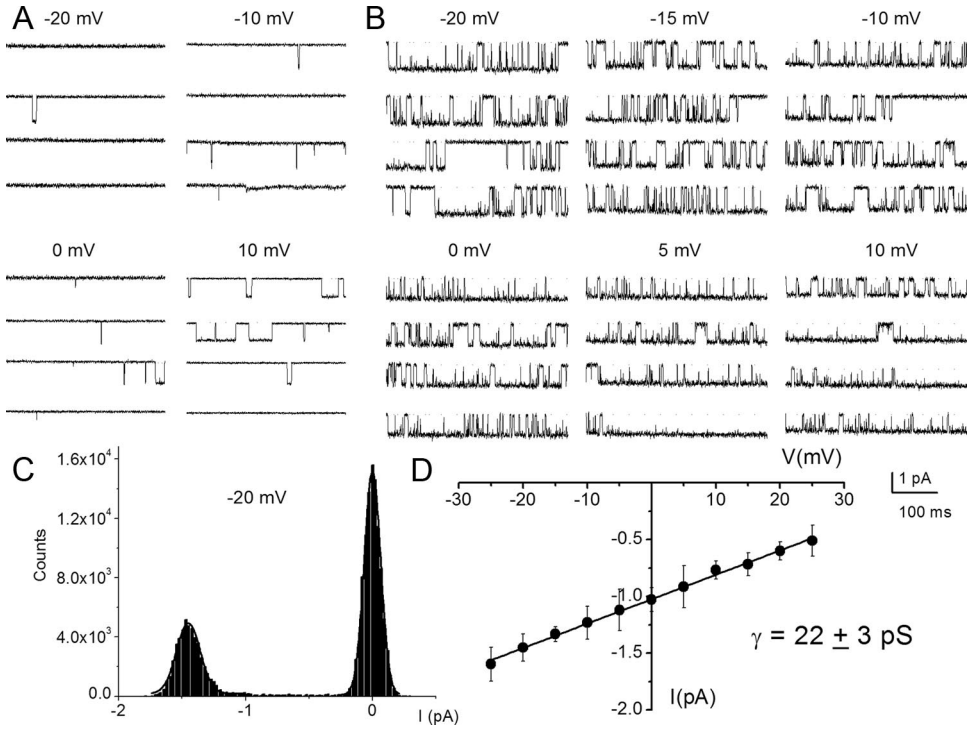

Figure 6. Effects of DHP Ca^{2+} channel agonist Bay K 8644 on single-channel Ca^{2+} currents. ***A***, Single-channel Ba^{2+} current traces were recorded in the cell-attached mode using 50 mM Ba^{2+} as the charge carrier. The traces were generated by holding the membrane patch at −70 mV and stepped to potentials indicated above each set of traces. The continuous dotted lines indicate the closed level. Downward steps indicate the opened level. Brief openings were more frequent than long openings in the unmodified channel. ***B***, Illustration of the effects of 5 μM Bay K 8644 on the same patch shown in ***A***. Bay K 8644 promoted long openings. While Bay K 8644 increased the frequency and duration of single-channel openings, nimodipine (10 μM) had the opposite effect (data not shown). ***C***, An example of amplitude histogram used to determine the mean magnitude of unitary currents at different step potentials. ***D***, Single-channel conductance (●) of L-type channel for Ba^{2+} was determined using linear least-square fits to the mean single-channel amplitude at different step potentials. The conductance of the L-type channel was 22 ± 3 pS ($n = 11$).

action potentials (Fig. 5*F*,*G*). Because suppression of T-type, P/Q-type, and R-type currents produces prolongation of action potential width and reduces the extent of the AHP, it can be inferred that activation of these Ca^{2+} currents may mediate activation of unidentified outward currents. The N-type Ca^{2+} current produces a modest effect on the action potential profile in addition to prolongation of the latency (Fig. 5*I*, Table 2). The use of 4-AP-modified action potentials conveniently allowed us to examine the contribution of distinct Ca^{2+} channel subtypes in spike waveforms. However, it is conceivable, albeit unlikely, that the use of different concentrations of 4-AP and/or other K^+ current blockers would have brought about a different outcome.

Unitary current properties of single-channel currents in SGNs

To further demonstrate that SGNs express multiple Ca^{2+} channel currents, we used a direct approach by recording from single-channel patches in the cell-attached configuration. Figure 6*A* shows a family of single-channel Ba^{2+} current traces recorded from a patch held at a holding potential of −70 mV and stepped to voltages indicated in control (Fig. 6*A*). The charge carrier was 50 mM Ba^{2+}. Membrane depolarization resulted in typical brief and long openings and, moreover, these long openings were favored at more depolarized potentials in controls and after application of Bay K 8644 (Fig. 6*B*). The amplitude histogram obtained from a test potential of −20 mV is shown (Fig. 6*C*). Illustrated in Figure 6*D* is the summary data of the unitary current amplitudes plotted against the test potentials for the DHP-sensitive Ca^{2+} channels. The slope conductance for the linear plot is 22 ± 3 pS ($n = 11$). Figure 7 is a layout of cell-attached patch recordings of a family of consecutive Bay K 8644-modified single-channel current traces recorded using 50 mM Ba^{2+} as the charge carrier from a holding potential of −70 mV and stepped to the −10 mV (left) and 0 mV (right). At more depolarized potentials the channel had frequent long openings, increasing the open probability that is readily visible in the diary plot (Fig. 7*C*) and in the well resolved increased magnitude of the ensemble-averaged currents (Fig. 7*B*). The activation of the L-type channel has steep voltage dependence, and a fit to the Boltzmann function revealed a half-activation voltage ($V_{½}$) of −9.5 ± 2.4 mV ($n = 7$) and a maximum slope factor (k) of 4.3 ± 1.2 mV ($n = 7$; Fig. 7*D*). Next, we examined the kinetics of the Bay K 8644-modified single L-type Ca^{2+} channels. To ensure that the recordings were made from single L-type channels, only patches containing single-channel events blocked by nimodipine were analyzed. Additionally, kinetic analyses were performed on patches that contained only one channel. The criteria consisted of quantitative determination followed by visual inspection of the data (Horn et al., 1991). The patches contained one channel because there was no stacking of events. Furthermore, direct transition from fast to slow kinetics showed similar current amplitude and vice versa, indicating that the gating modes were derived from a single channel. In accordance with a voltage-dependent channel, the time constant of the first latency was faster at more depolarized voltage than hyperpolarized voltage steps (Fig. 7*E*). Figure 7*F*,*G* shows open and closed time distributions of single Ba^{2+} channel currents. Using 50 mM Ba^{2+} as the charged carrier, the channel gating could be described by at least two open and closed states. However, at some step potentials, the fast closed time could not be resolved. As shown, for a Bay K 8644-modified channel, patch

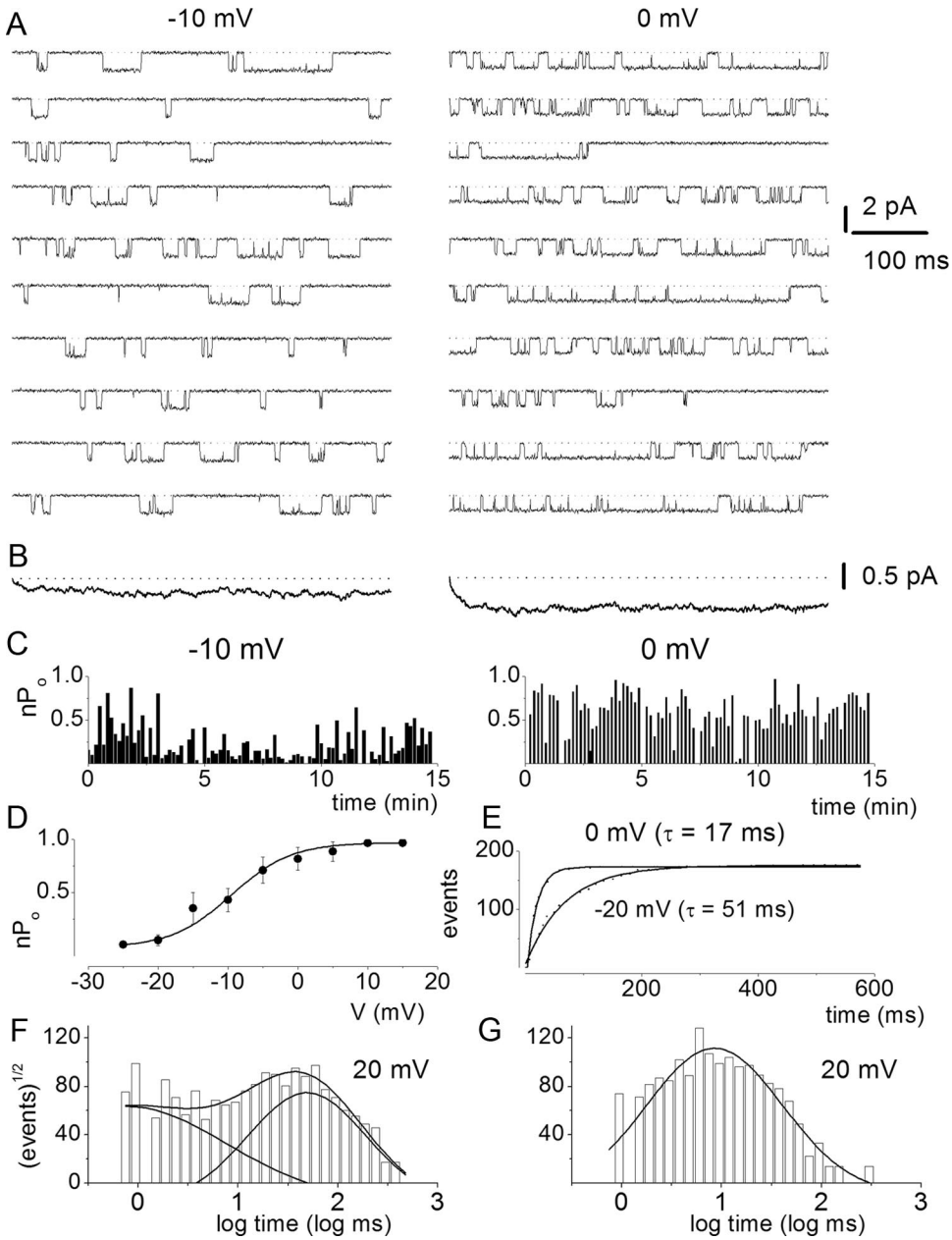

Figure 7. Voltage dependence of L-type single-channel currents in adult SGNs. ***A***, Representative consecutive single-channel traces of Ba^{2+} currents at test potentials −10 and 0 mV were obtained from L-type channel using the agonist Bay K 8644 (5 μM) in the bath solution. Ten consecutive traces are shown at the step potentials indicated, from a holding potential of −70 mV. ***B***, Ensemble-averaged currents at a given test potential were constructed from idealized current traces from ~400 consecutive sweeps. The ensemble-averaged current traces derived are shown at the bottom of each column of traces. ***C***, Diary of the channel open probability at test potentials (Po) of −10 and 0 mV. ***D***, Pos versus voltage relation for L-type channels were obtained from 500 ms voltage steps ranging from −25 to 15 mV. Each symbol represents the mean Po (including null traces) determined from 400 consecutive sweeps. The continuous solid line represents a single Boltzmann function fit to the data points. The half-activation voltage ($V_{1/2}$) was −9.5 ± 2.4 mV ($n = 7$) and the slope factor of 4.3 ± 1.2 mV ($n = 7$). ***E***, Voltage dependence of first-latency distribution in single-channel Ba^{2+} currents. Cumulative first-latency distribution plots were generated from the waiting time to first opening as a function of time, at the step voltages indicated. Exponential fits to the first-latency distribution are drawn with solid lines. Time constants of the first-latency distribution (τ) are indicated. ***F***, ***G***, Dwell time histograms were binned logarithmically using 10 bins per decade and plotted with a square root transformation of the number of events. Open (***F***) and closed (***G***) time distribution were fitted with two open ($\tau o1$ and $\tau o2$) and two closed ($\tau c1$ and $\tau c2$) time constants, respectively. However, at some step voltages as shown (20 mV), the fast closed dwell time constant could not be resolved. For example, at 0 mV step voltage: $\tau o1$, 1.7 ± 0.6 ms, $n = 5$; $\tau o2$, 37.0 ± 6.1 ms, $n = 5$; $\tau c1$, 0.6 ± 0.1 ms, $n = 5$; $\tau c2$, 13.2 ± 4.7 ms, $n = 5$. Moreover, at 20 mV step voltage: $\tau o1$, 0.8 ± 0.3 ms, $n = 6$ (17%); changes $\tau o2$, 48.0 ± 6 ms, $n = 6$ (83%); τc, 8.5 ± 1.2 ms, $n = 6$. The numbers in parentheses represent the percentage of time in which the channel dwells at the different states.

depolarization increased the duration of long open states as gleaned from the relative dwell times of each component.

We surmised that by exposing SGNs to specific Ca^{2+} channel blocker mixtures, it should be feasible to resolve the single-channel fluctuations of other Ca^{2+} current subtypes identified at the whole-cell current level. To record N-type single-channel Ba^{2+} currents, we included a mixture of Ca^{2+} channel blockers consisting of 10 μM nimodipine, 1 μM ATX, 200 nM ω-theraphotoxin-Hg1a, ω-(rSNX-482), and 5 μM mibefradil in the external and patch-electrode solutions. The patch pipette contained 50 mM Ba^{2+}. As shown in Figure 8*A*, the resulting consecutive single-channel fluctuation traces at different test potentials displayed inward currents that were invariably sustained at test potentials ranging from −10 to 5 mV, from a holding

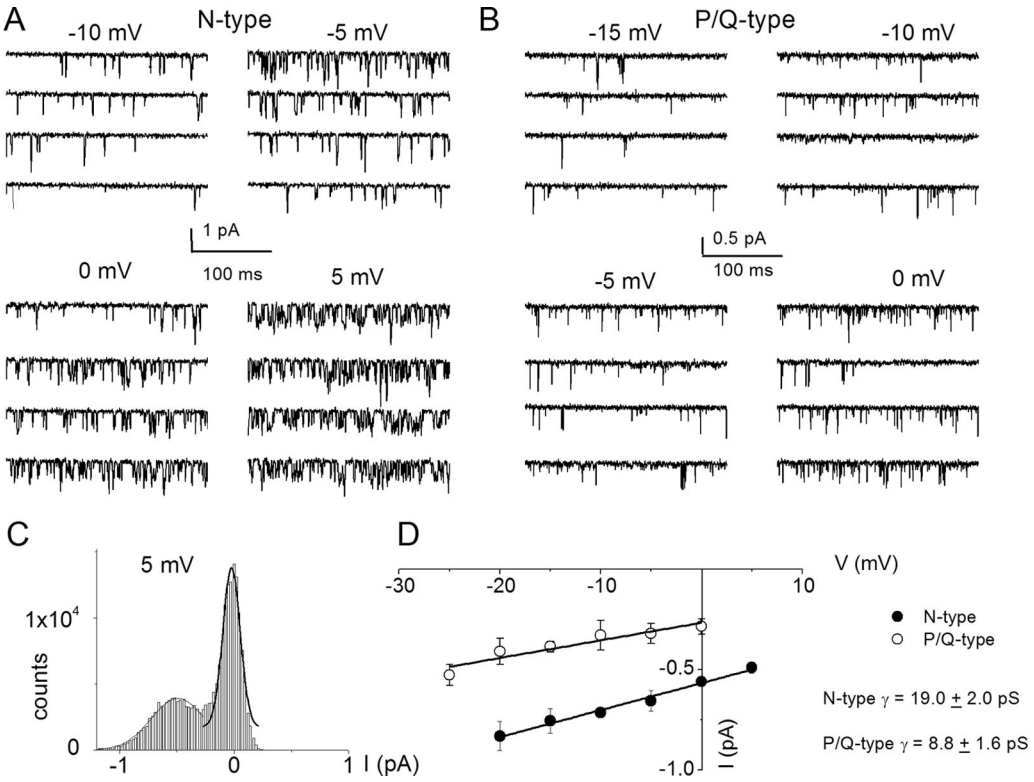

Figure 8. Single-channel recordings of N-type and P/Q-type channels in SGNs. ***A***, Inward Ba^{2+} currents through single Ca^{2+} channels were recorded in membrane patches from isolated 3-month-old SGNs. For recordings of N-type single-channel activity, we included a mixture of Ca^{2+} channel blockers containing the following: 10 μM nimodipine, 1 μM ATX, 200 nM ω-(rSNX-482), and 5 μM mibefradil in the external and patch-electrode solutions. The membrane patch was held at −70 mV and stepped to test voltages indicated above each set of four consecutive traces. The solid dotted lines denote the closed levels. The test potential for the example shown is 5 mV. ***C***, Representative I–V plots for N-type channels show single-channel conductance of 19 ± 2 pS (n = 7). ***B***, To record the unitary P/Q-type single-channel fluctuations, we included a mixture of Ca^{2+} channel blockers containing the following: 10 μM nimodipine, 1 μM CTX, 200 nM ω-(rSNX-482), and 5 μM mibefradil in the external and patch-electrode solutions. Under outside-out cell-attached configuration, 3-month-old SGN membrane patches were held at −70 mV and stepped to the depolarizing potentials, as indicated beside the family of consecutive traces. We used 50 mM Ba^{2+} as the charge carrier. ***C***, The amplitude histogram from current traces at 5 mV step potential is shown. Similar data were used to generate the unitary I–V plots. ***D***, The scattered points of the I–V relation were fitted with a linear regression to determine the conductance of the P/Q channels. For the summary data shown, the single-channel conductance (γ) values for P/Q-type channels in 50 mM Ba^{2+} is 8.8 ± 1.6 pS (n = 6).

potential of −70 mV. An example of the amplitude histograms used to generate the unitary current amplitude is shown (Fig. 8*C*). The estimated single-channel conductance from the regression line of the I–V relationship was 19 ± 2 pS (n = 7) (Fig. 8*D*). Similar experiments were performed to record P/Q-type single-channel Ba^{2+} currents (Fig. 8*B*). The unitary P/Q-type currents were recorded in bath and patch-pipette solutions containing 10 μM nimodipine, 1 μM CTX, 200 nM ω-(rSNX-482), and 5 μM mibefradil to suppress other Ca^{2+} channel currents. As shown, the resulting current had openings that were brief and persistent, and the ensuing single-channel conductance generated from the regression line of the I–V relationship was 8.8 ± 1.6 pS (n = 6) (Fig. 8*D*). Finally, single-channel Ba^{2+} currents from T-type and R-type channels were recorded using external and pipette solutions, which suppressed other Ca^{2+} channel subtypes except T-type and R-type channels (Fig. 9, legend). Single-channel Ba^{2+} currents flowing through T-type channels were recorded with external and pipette solutions containing 10 μM nimodipine, 1 μM CTX, 200 nM ω-(rSNX-482), and 1 μM ATX. Using 50 mM Ba^{2+} as the charge carrier, cell-attached patches held at a holding potential of −90 mV and step potentials displayed inward currents that were invariably transient (Fig. 9*A*). The family of recordings illustrated is from consecutive traces. In another set of experiments when the external and patch pipette solution contained 10 μM nimodipine, 1 μM CTX, 5 μM mibefradil, and 1 μM ATX, the unitary currents had brief openings but persisted throughout the duration of the step voltages. We inferred that these single-channel events resulted from the activity of R-type channels in adult SGNs. Figure 9*B* shows R-type single-channel current traces recorded from a holding potential of −70 mV and the step potentials noted above each set of five consecutive traces. The estimated single-channel conductances from the regression lines of the I–V relationship (Fig. 9*C*) were 9.5 ± 1.3 pS (n = 5) and 14.9 ± 2.8 pS (n = 6), for T-type and R-type channels, respectively.

Localization of Ca^{2+} channel protein in SGNs

We proceeded to identify Ca^{2+} channel subtypes expressed in SGNs using immunofluorescence microscopic methods. We used antibodies against Cav1.3, Cav2.1, Cav2.2, and Cav2.3, and observed positive labeling in the membrane and cytoplasm of SGNs in both apical and basal neurons (Fig. 10). In control experiments whereby SGNs were preincubated with purified peptides supplied by the company (data not shown), positive labeling was absent, indicating that the antibodies recognized the targeted sequence. The specificity of the antibodies was not confirmed, however. Using anti-Cav3.1–3 antibodies, we detected consistent positive labeling of the membrane and cytoplasm of apical and basal SGNs (Fig. 10). The labeling was abolished when antibodies were preincubated with purified peptides of the respective Cav3.1, Cav3.2, and Cav3.3 channels. The expression of the different Ca^{2+} channel subtypes in the plasma membrane and cy-

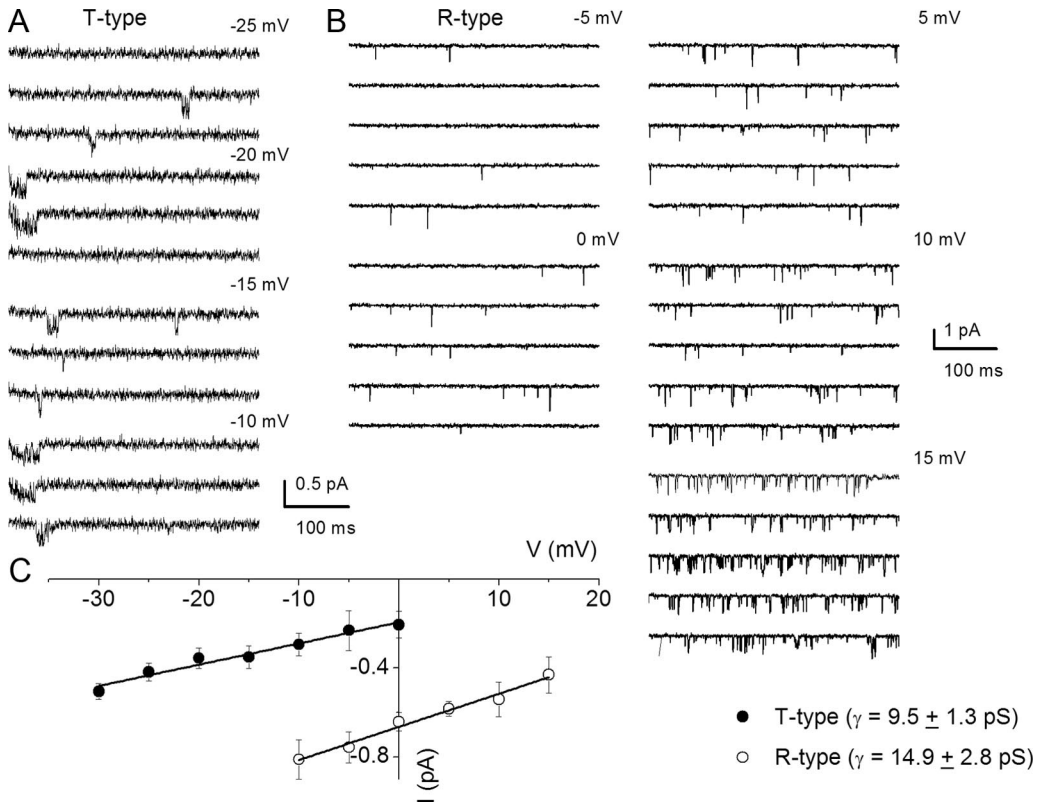

Figure 9. Single-channel conductance of T-type and R-type Ca^{2+} channels in adult SGNs. ***A***, Representative and consecutive single-channel traces recorded in a cell-attached patch with pipette solution containing 50 mM Ba^{2+}. Additionally, the patch-pipette and bath solution consisted of a mixture of Ca^{2+} channel blockers: 10 μM nimodipine, 1 μM CTX, 200 nM ω-(rSNX-482), and 1 μM ATX. The holding potential was −90 mV and the step potentials are indicated. ***B***, To examine the unitary current fluctuations of R-type Ca^{2+} channels, we included a mixture of Ca^{2+} channel blockers containing the following: 10 μM nimodipine, 1 μM CTX, 5 μM mibefradil, and 1 μM ATX in the bath and pipette solutions. Shown are sets of families of consecutive single-channel sweeps recorded in the cell-attached configuration, using 50 mM Ba^{2+} as the charge carrier. The membrane patch was held at a holding potential of −70 mV and stepped to potentials denoted above each set of sweeps. ***C***, The I–V relationships are shown for T-type and R-type unitary currents, respectively. The single-channel conductances were as follows: T type, 9.5 ± 1.3 pS, $n = 5$; R-type, 14.9 ± 2.8 pS, $n = 6$.

toplasm is illustrated in Figure 11. To ensure that the data obtained from isolated neurons *in vitro* reflected well with *in vivo* conditions, we repeated the experiments using cryosections of the cochlea (Fig. 12), confirming the existence of multiple Ca^{2+} channels in adult SGNs. Thus, biophysical, pharmacological, and biochemical analyses divulged from these studies strongly suggest that adult SGNs employ multiple Ca^{2+} channel currents to confer diverse Ca^{2+}-dependent functions.

Discussion

The input and output functions of prehearing SGNs are distinct from posthearing neurons. On one hand, the functional coding of action potentials and the wiring of synaptic connections in prehearing neurons are thought to be shaped by spontaneous activity from immature hair cells (Kros et al., 1998; Beutner and Moser, 2001; Marcotti et al., 2003; Levic et al., 2007; Tritsch et al., 2007). Moreover, outputs from SGNs to the CN also determine the wiring pattern and neuronal morphology in the brainstem (Deitch and Rubel, 1989a,b; Pasic and Rubel, 1989). These findings underpin the concept that the activity of prehearing hair cells and SGNs may sculpt their niche in the constellation of neuronal networks in the auditory pathway. On the other hand, the activity of posthearing SGNs should match markedly well with rapid and graded receptor potential from hair cells (Palmer and Russell, 1986). At the pivot of the multiple functions of the posthearing SGN is the contribution of Ca^{2+} in shaping the coding pattern by way of Ca^{2+} currents and in the activation of Ca^{2+}-dependent ionic currents.

The diversity of Ca^{2+} currents in SGNs abounds. The implicit assertion from previous reports suggests that, because the physiological requisite for Ca^{2+}-dependent functions varies in posthearing SGNs, Ca^{2+} currents and Ca^{2+} handling in SGNs may differ from prehearing neurons. Whereas the α-subunit of Cav2.1 was expressed robustly in prehearing mouse SGNs, it was undetected in adult chinchilla neurons (Lopez et al., 2003; Chen et al., 2011). To ensure accurate representation of the frequency map of the cochlea, the properties of type-1 SGNs vary depending on their apicobasal location (Rusznák et al., 2008; Rusznák and Szucs, 2009). Differences in the membrane properties of apical versus basal SGNs have been ascribed to differential expression of distinct K^+ channels, yielding two distinct cell types, namely fast-adapting and slow-adapting neurons (Adamson et al., 2002b; Beisel et al., 2005; Chen and Davis, 2006; Bakondi et al., 2009).

First, in contrast to prehearing SGNs where the neurons have been categorized into fast-adapting and slow-adapting neurons, posthearing neurons are seemingly heterogenous in their firing patterns. In adult neurons, firing patterns range widely, from spontaneously active to quiescent. These patterns, when invoked, result in fast-adapting, moderately adapting, and slowly adapting neurons. Indeed SGNs from postnatal day 0–5 mice have been demonstrated to have intrinsic spontaneous firing (Lin and

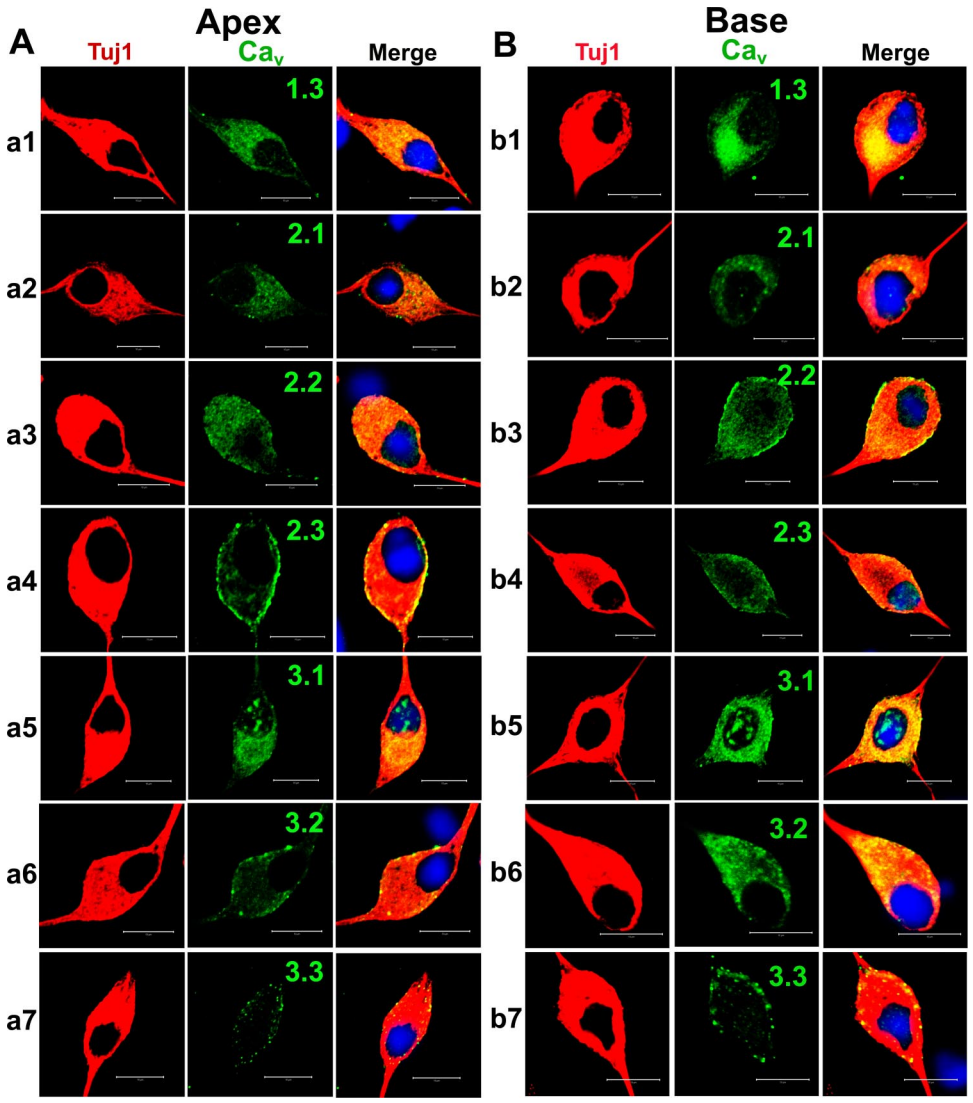

Figure 10. Cultured SGNs express multiple Ca^{2+} channels. ***A***, Cultured (48 h in culture) apical SGNs were fixed and labeled with antibodies against Cav1.3, Cav2.1, Cav2.2, Cav2.3, Cav3.1, Cav3.2, and Cav3.3. As shown, neurons were labeled with the neuronal marker Tuj1 (***a1***–***a7***, left, red), the channels (middle, green), and the nuclei were stained with DAPI (blue) and the images merged (right). SGNs stained positively for Cav1.3, Cav2.1, Cav2.2, Cav2.3, Cav3.1, Cav3.2, and Cav3.3. ***B***, Similar data were obtained for basal neurons as shown in ***b1***–***b7*** for Tuj1, nuclei stain, and channels Cav1.3, Cav2.1, Cav2.2, Cav2.3, Cav3.1, Cav3.2, and Cav3.3, respectively. Scale bar, 10 μm.

Chen, 2000). The firing pattern of adult neurons and their place map along the cochlear contour appears not as distinct as has been reported for prehearing neurons (Adamson et al., 2002b; Chen and Davis, 2006). Data presented in Figure 1*A*,*D* suggest that Ca^{2+} channels constitute ~50% of the spike amplitude. Moreover, the effects of nominal Ca^{2+} (~100 μM), specifically spike overshoots, were masked in experiments using nanomolar Ca^{2+}. Mg^{2+} substitution for Ca^{2+} might have eliminated surface charge screening effects of divalent cations. However, other effects of Mg^{2+} on Na^+ and K^+ currents are likely to mask the genuine effects of the reduction of external Ca^{2+} (Negulyaev and Markwardt, 2000; Murata et al., 2002). Additionally, the voltage dependence of activation and inactivation of Na^+ currents depends on Ca_i^{2+} modulation (Biswas et al., 2009). Na^+ channels are exquisitely sensitive to available Ca_i^{2+} (Horn, 1999; Wingo et al., 2004). Thus, it is plausible to speculate that by reducing external Ca^{2+}, Na^+ currents may be enhanced, producing an aberrant increase in the action potential overshoot.

Second, we have recently used strategies to isolate adult mice SGNs (Lv et al., 2010) and, in this report, have described in detail the composition of multiple Ca^{2+} currents in posthearing neurons. The findings are as follows:

1. The magnitude of Ca^{2+} current density was markedly larger in posthearing SGNs at the apical rather than at the basal turn of the cochlea.
2. Evidence for functional expression of multiple Ca^{2+} currents in adult SGNs can be gleaned from disparate closing kinetics of the whole-cell Ca^{2+} currents (Armstrong and Matteson, 1985, 1986).
3. Voltage-dependent activation/deactivation and inactivation criteria, as well as pharmacological indexes, have further ascertained that adult SGNs harbor Cav1.3 (L type), Cav2.1 (P/Q type), Cav2.2 (N type), and Cav2.3 (R type) channels (Catterall et al., 2005) (Table 3). These channels constitute ~70 and 80% of the total Ca^{2+} currents at basal and apical turns of the cochlea, respectively. The remaining current may be derived from Cav3 (T type) channels.
4. Data gleaned from pharmacological dissection of posthearing SGNs dovetailed well with the *in vitro* and *in vivo*

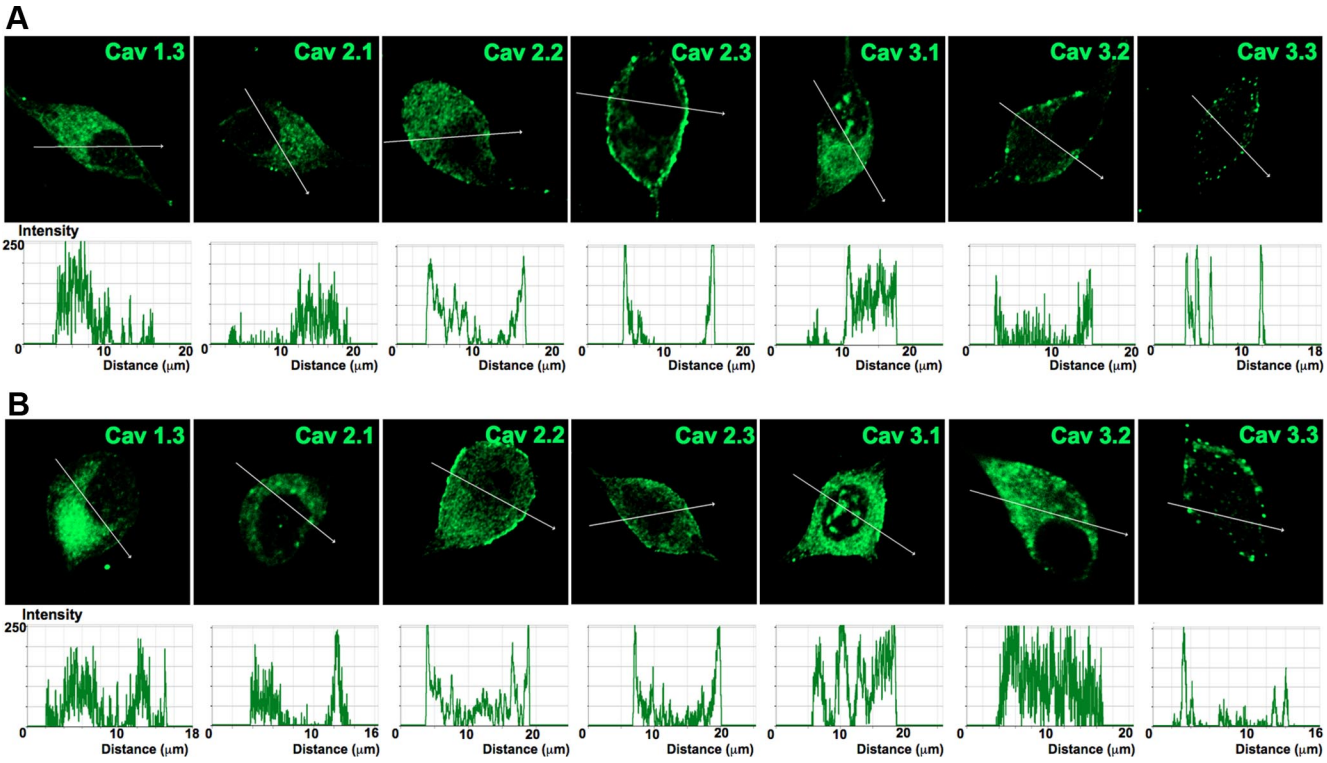

Figure 11. Profile of Ca^{2+} channel expression in plasma membrane and cytosol of adult SGNs. To gauge the membrane expression of Ca^{2+} channels in SGNs, we assembled data from Figure 10 and plotted fluorescent intensity with respective distance across the diameter of neurons. ***A***, ***B***, Expression pattern of Ca^{2+} channels in apical neurons (***A***) and basal neurons (***B***). Scale bar, 10 μm.

immunolabeling analyses. A note of caution on the pharmacological analysis should be highlighted, however, as some of the Ca^{2+} channel blockers (e.g., the DHPs) have been found to block K^+ currents as well. Thus, the nonspecific effects of the Ca^{2+} channel blockers cannot be ruled out (Zhang and Gold, 2009). Blockage of Ca^{2+} currents may produce functional alteration of the Ca^{2+}-activated K^+ current (I_{KCa}), which may be manifested as increased neuronal excitability (Gu et al., 2007). Alternatively, enhanced I_{KCa} can produce similar effects by inducing membrane hyperpolarization, resulting in removal of Na^+ channels from inactivation (Du et al., 2005). Moreover, the proximity of I_{KCa} channels and the effectiveness of $Ca^{2+}{}_i$ buffers can play important roles in the physiological outcomes.

5. The L-type and N-type currents may be disproportionately expressed along the tonotopic axis of the cochlea, such that apical neurons express substantially larger currents than basal neurons. If spike frequency adaptation in SGNs is Ca^{2+} dependent via I_{KCa}, as has been documented in other systems (Lorenzon and Foehring, 1992; Kim and Rieke, 2001; Groth et al., 2011), it would be consistent with the finding that apical neurons express larger Ca^{2+} current magnitude than basal neurons.
6. By measuring the single-channel fluctuations of Ca^{2+} channel current subtypes, we have demonstrated that the L-type, N-type, P/Q-type, R-type, and T-type channels in adult SGNs are distinct with conductance of ~22, 19, 9, 15, and 10 pS, respectively. Differences in conductances invariably result from the concentrations and divalent cations used as charge carriers for Ca^{2+} channels (Church and Stanley, 1996; Rodriguez-Contreras and Yamoah, 2001; 2002, 2008). The concentration of Ba^{2+} (50 mM) used as a charge carrier is expected to impose a surface charge effect, producing a rightward shift in the voltage dependence of activation (Hagiwara and Takahashi, 1967). The $V_{½}$ obtained for the L-type channel (−9.5 ± 2.4 mV) would be expected to shift by ~18 mV in the hyperpolarized direction if the experiments were conducted in 5 mM Ba^{2+}, resulting in values comparable to those of previous reports on the L-type channels in hair cells from the bullfrog saccule (Rodríguez-Contreras and Yamoah, 2003) and mouse cochlear hair cells (Zampini et al., 2010).

Differential and heterogenous expression of Ca^{2+} channels along the frequency map of the cochlea of prehearing SGNs have been demonstrated and, similar to previous studies, the expressions of Cav1.3, Cav2.2, and Cav3.3 have been confirmed to be neuron-specific (Chen et al., 2011). In contrast, posthearing SGNs have been shown to express additional Ca^{2+} channels, namely Cav1.2 and Cav3.1 (Lopez et al., 2003). A recent report has demonstrated that ~90% of the presynaptic Ca^{2+} currents of postnatal day 11 SGNs at the bushy cell synapse is of the P/Q type (Lin et al., 2011). Thus, differential expression of Ca^{2+} channel subtypes, as seen along the cochlear contour, may also take place along the soma–axonal axis of SGNs. The complex distribution pattern of Ca^{2+} channels in SGNs is underpinned by the findings that Schwann cell ensheathments of neurons are also endowed with multiple Ca^{2+} channels (Chen et al., 2011), making it difficult, especially when immunolabeling is only used in the *in vivo* setting, to distinguish between neuron versus Schwann cell-specific Ca^{2+} channel subtypes. In this study, we circumvent the masking effects of glial-cell Ca^{2+} currents, since dissociated SGNs lose their glial cell after ~48 h. Thus, our study unequivocally demonstrates that SGNs express at least five distinct Ca^{2+} channels.

Control of Ca^{2+} channel currents and spatial and temporal separation of Ca^{2+} signaling pathways is achieved by several

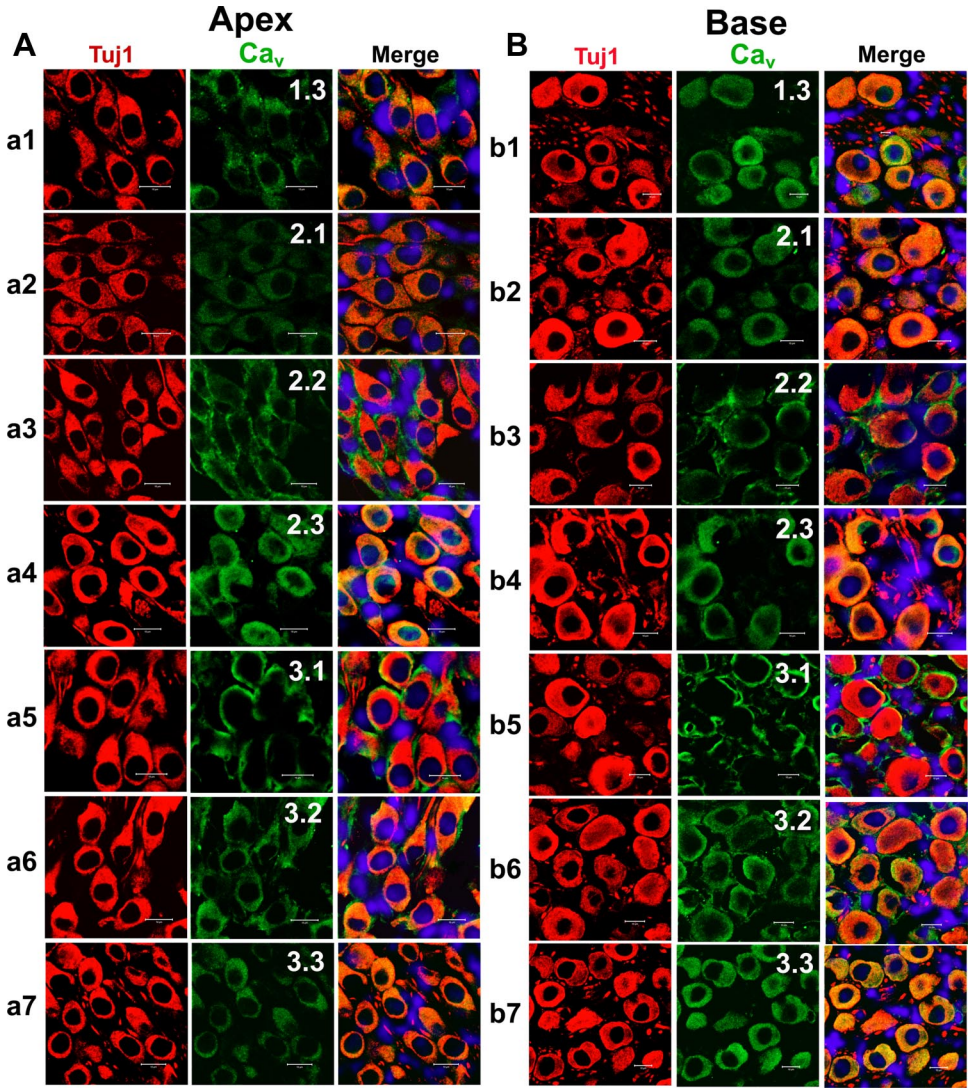

Figure 12. Expression of Cav1.3, Cav2.1, Cav2.2, Cav2.3, Cav3.1, Cav3.2, and Cav3.3 in mouse cochlea sections. ***A***, ***B***, To rule out the possibility that both apical (***A***) and basal (***B***) SGNs expressed Ca^{2+} channels *in vivo* when compared with the cell culture-induced expression of channels, we performed immunolabeling as described in Figure 10 on sections of the cochlea from a 3-month-old mice. Apical SGNs were labeled with antibodies against Cav1.3, Cav2.1, Cav2.2, Cav2.3, Cav3.1, Cav3.2, and Cav3.3. Neurons were labeled with the neuronal marker Tuj1 (red). The channels (green) and the nuclei (blue) were stained with DAPI. Images were merged (right). SGNs stained positively to Cav1.3, Cav2.1, Cav2.2, Cav2.3, Cav3.1, Cav3.2, and Cav3.3. ***B***, Similar data were obtained for basal neurons as shown for Cav1.3, Cav2.1, Cav2.2, Cav2.3, Cav3.1, Cav3.2, and Cav3.3, respectively. Scale bar, 10 μm.

Table 3. Comparison of previous reports on Ca^{2+} currents/channels in SGNs

Reference	Preparation	Current/s	Sensitivity	α-Subunit	Methods	Predicted functions
Lv et al. (this paper)	Posthearing murine SGNs	L, N, P/Q, RT types	Cd^{2+}, DHPs, CTX, ATX, rSNX482, mibefradil	$Ca_v1.3$, $Ca_v2.1$–3, $Ca_v3.1$–3	EP, IC, WCVC, SC/IM	Spike latency, amplitude, width, AHP spike frequency, pattern activation of outward currents
Chen et al., 2011	Prehearing murine SGNs	N/A	Cd^{2+}	$Ca_v1.3$, $Ca_v2.2$, $Ca_v3.3$	EP, IC/IM	
Lopez et al., 2003	Posthearing chinchilla SGNs	N/A	N/A		IM	Spike shape of APs
Jimenez et al., 1997	Embryonic day 6–17 chicks	L, N types	Cd^{2+}, DHPs, ω-conotoxin GVIA	N/A	EP, WCVC	Neuronal development
Hisashi et al., 1995	Posthearing guinea pig SGNs	L type	La^{3+}, Cd^{2+}, Ni^{2+}, Co^{2+}, DHPs	N/A	EP, WCVC	Spike shape of APs

EP, electrophysiology; IC, current clamp; WCVC, whole-cell voltage clamp; SC, single-channel recordings; IM, immunolocalization; AP, action potential.

means, including fixed and diffusible endogenous Ca^{2+} buffers, Ca^{2+} stores, and Ca^{2+} extrusion mechanisms (Meinrenken et al., 2003). An alternative mechanism is to assign different Ca^{2+} channel domains to diverse functions through Ca^{2+} channel clusters and Ca^{2+} channel subtypes (Rodriguez-Contreras and Yamoah, 2001). In contrast to hair cells, in which the predominant Ca^{2+} currents is derived from neuronal Cav1.3 channel currents (Platzer et al., 2000; Rodriguez-Contreras and Yamoah, 2001; Dou et al., 2004; Zampini et al., 2010), SGNs employ multiple Ca^{2+} currents to confer Ca^{2+}-dependent functions. These functions range from sculpting the shape, duration, and modulation of K^+ currents to determining the contour of AHP of action potentials. At the presynaptic sites, Ca^{2+}-mediated transmitter release can be conferred by a few distinct channels (Borst

and Sakmann, 1999; Lin et al., 2011). Moreover, the potential role of Ca^{2+} channels (e.g., $Ca_v1.2$ channels) in excitation–transcription coupling in SGNs may require future investigations (Dolmetsch et al., 2001; Marshall et al., 2011). Thus, the next phase of understanding Ca^{2+}-mediated signaling in SGNs would be to identify Ca^{2+} channel subtype-specific functions.

References

Adamson CL, Reid MA, Davis RL (2002a) Opposite actions of brain-derived neurotrophic factor and neurotrophin-3 on firing features and ion channel composition of murine spiral ganglion neurons. J Neurosci 22:1385–1396. Medline

Adamson CL, Reid MA, Mo ZL, Bowne-English J, Davis RL (2002b) Firing features and potassium channel content of murine spiral ganglion neurons vary with cochlear location. J Comp Neurol 447:331–350. CrossRef Medline

Armstrong CM, Matteson DR (1985) Two distinct populations of calcium channels in a clonal line of pituitary cells. Science 227:65–67. CrossRef Medline

Armstrong CM, Matteson DR (1986) The role of calcium ions in the closing of K channels. J Gen Physiol 87:817–832. CrossRef Medline

Bakondi G, Pór A, Kovacs I, Szucs G, Rusznák Z (2009) Hyperpolarization-activated, cyclic nucleotide-gated, cation nonselective channel subunit expression pattern of guinea-pig spiral ganglion cells. Neuroscience 158:1469–1477. CrossRef Medline

Bar-Yehuda D, Korngreen A (2008) Space-clamp problems when voltage clamping neurons expressing voltage-gated conductances. J Neurophysiol 99:1127–1136. CrossRef Medline

Bean BP (1984) Nitrendipine block of cardiac calcium channels: high-affinity binding to the inactivated state. Proc Natl Acad Sci U S A 81:6388–6392. CrossRef Medline

Beisel KW, Rocha-Sanchez SM, Morris KA, Nie L, Feng F, Kachar B, Yamoah EN, Fritzsch B (2005) Differential expression of KCNQ4 in inner hair cells and sensory neurons is the basis of progressive high-frequency hearing loss. J Neurosci 25:9285–9293. CrossRef Medline

Beutner D, Moser T (2001) The presynaptic function of mouse cochlear inner hair cells during development of hearing. J Neurosci 21:4593–4599. Medline

Biswas S, DiSilvestre D, Tian Y, Halperin VL, Tomaselli GF (2009) Calcium-mediated dual-mode regulation of cardiac sodium channel gating. Circ Res 104:870–878. CrossRef Medline

Borst JG, Sakmann B (1999) Effect of changes in action potential shape on calcium currents and transmitter release in a calyx-type synapse of the rat auditory brainstem. Philos Trans R Soc Lond B Biol Sci 354:347–355. CrossRef Medline

Catterall WA, Perez-Reyes E, Snutch TP, Striessnig J (2005) International Union of Pharmacology. XLVIII. Nomenclature and structure-function relationships of voltage-gated calcium channels. Pharmacol Rev 57:411–425. CrossRef Medline

Chen WC, Davis RL (2006) Voltage-gated and two-pore-domain potassium channels in murine spiral ganglion neurons. Hear Res 222:89–99. CrossRef Medline

Chen WC, Xue HZ, Hsu YL, Liu Q, Patel S, Davis RL (2011) Complex distribution patterns of voltage-gated calcium channel alpha-subunits in the spiral ganglion. Hear Res 278:52–68. CrossRef Medline

Church PJ, Stanley EF (1996) Single L-type calcium channel conductance with physiological levels of calcium in chick ciliary ganglion neurons. J Physiol 496:59–68. Medline

Deitch JS, Rubel EW (1989a) Changes in neuronal cell bodies in N. laminaris during deafferentation-induced dendritic atrophy. J Comp Neurol 281:259–268. CrossRef Medline

Deitch JS, Rubel EW (1989b) Rapid changes in ultrastructure during deafferentation-induced dendritic atrophy. J Comp Neurol 281:234–258. CrossRef Medline

Dolmetsch RE, Pajvani U, Fife K, Spotts JM, Greenberg ME (2001) Signaling to the nucleus by an L-type calcium channel-calmodulin complex through the MAP kinase pathway. Science 294:333–339. CrossRef Medline

Dou H, Vazquez AE, Namkung Y, Chu H, Cardell EL, Nie L, Parson S, Shin HS, Yamoah EN (2004) Null mutation of alpha1D Ca^{2+} channel gene results in deafness but no vestibular defect in mice. J Assoc Res Otolaryngol 5:215–226. Medline

Du W, Bautista JF, Yang H, Diez-Sampedro A, You SA, Wang L, Kotagal P, Lüders HO, Shi J, Cui J, Richerson GB, Wang QK (2005) Calcium-sensitive potassium channelopathy in human epilepsy and paroxysmal movement disorder. Nat Genet 37:733–738. CrossRef Medline

Groth RD, Lindskog M, Thiagarajan TC, Li L, Tsien RW (2011) Beta Ca2+/CaM-dependent kinase type II triggers upregulation of GluA1 to coordinate adaptation to synaptic inactivity in hippocampal neurons. Proc Natl Acad Sci U S A 108:828–833. CrossRef Medline

Gu N, Vervaeke K, Storm JF (2007) BK potassium channels facilitate high-frequency firing and cause early spike frequency adaptation in rat CA1 hippocampal pyramidal cells. J Physiol 580:859–882. CrossRef Medline

Hagiwara S, Takahashi K (1967) Surface density of calcium ions and calcium spikes in the barnacle muscle fiber membrane. J Gen Physiol 50:583–601. CrossRef Medline

Hamill OP, Marty A, Neher E, Sakmann B, Sigworth FJ (1981) Improved patch-clamp techniques for high-resolution current recording from cells and cell-free membrane patches. Pflugers Arch 391:85–100. CrossRef Medline

Hegarty JL, Kay AR, Green SH (1997) Trophic support of cultured spiral ganglion neurons by depolarization exceeds and is additive with that by neurotrophins or cAMP and requires elevation of $[Ca^{2+}]i$ within a set range. J Neurosci 17:1959–1970. Medline

Helton TD, Xu W, Lipscombe D (2005) Neuronal L-type calcium channels open quickly and are inhibited slowly. J Neurosci 25:10247–10251. CrossRef Medline

Hisashi K, Nakagawa T, Yasuda T, Kimitsuki T, Komune S, Komiyama S (1995) Voltage-dependent Ca2+ channels in the spiral ganglion cells of guinea pig cochlea. Hear Res 91:196–201. CrossRef Medline

Horn F, Bilezikjian LM, Perrin MH, Bosma MM, Windle JJ, Huber KS, Blount AL, Hille B, Vale W, Mellon PL (1991) Intracellular responses to gonadotropin-releasing-hormone in a clonal cell-line of the gonadotrope lineage. Mol Endocrinol 5:347–355. CrossRef Medline

Horn R (1999) The dual role of calcium: pore blocker and modulator of gating. Proc Natl Acad Sci U S A 96:3331–3332. CrossRef Medline

Jagger DJ, Housley GD (2002) A-type potassium currents dominate repolarisation of neonatal rat primary auditory neurones in situ. Neuroscience 109:169–182. CrossRef Medline

Jagger DJ, Housley GD (2003) Membrane properties of type II spiral ganglion neurones identified in a neonatal rat cochlear slice. J Physiol 552:525–533. CrossRef Medline

Jiménez C, Giréldez F, Represa J, García-Díaz JF (1997) Calcium currents in dissociated cochlear neurons from the chick embryo and their modification by neurotrophin-3. Neuroscience 77:673–682. CrossRef Medline

Kim KJ, Rieke F (2001) Temporal contrast adaptation in the input and output signals of salamander retinal ganglion cells. J Neurosci 21:287–299. Medline

Kros CJ, Ruppersberg JP, Rüsch A (1998) Expression of a potassium current in inner hair cells during development of hearing in mice. Nature 394:281–284. CrossRef Medline

Leake PA, Hradek GT, Snyder RL (1999) Chronic electrical stimulation by a cochlear implant promotes survival of spiral ganglion neurons after neonatal deafness. J Comp Neurol 412:543–562. CrossRef Medline

Levic S, Nie L, Tuteja D, Harvey M, Sokolowski BH, Yamoah EN (2007) Development and regeneration of hair cells share common functional features. Proc Natl Acad Sci U S A 104:19108–19113. CrossRef Medline

Lewis RS, Hudspeth AJ (1983) Voltage- and ion-dependent conductances in solitary vertebrate hair cells. Nature 304:538–541. CrossRef Medline

Lin KH, Oleskevich S, Taschenberger H (2011) Presynaptic Ca2+ influx and vesicle exocytosis at the mouse endbulb of Held: a comparison of two auditory nerve terminals. J Physiol 589:4301–4320. Medline

Lin X, Chen S (2000) Endogenously generated spontaneous spiking activities recorded from postnatal spiral ganglion neurons in vitro. Brain Res Dev Brain Res 119:297–305. Medline

Lopez I, Ishiyama G, Acuna D, Ishiyama A, Baloh RW (2003) Immunolocalization of voltage-gated calcium channel alpha1 subunits in the chinchilla cochlea. Cell Tissue Res 313:177–186. CrossRef Medline

Lorenzon NM, Foehring RC (1992) Relationship between repetitive firing and afterhyperpolarizations in human neocortical neurons. J Neurophysiol 67:350–363. Medline

Lv P, Wei D, Yamoah EN (2010) Kv7-type channel currents in spiral ganglion neurons: involvement in sensorineural hearing loss. J Biol Chem 285:34699–34707. CrossRef Medline

Marcotti W, Johnson SL, Rusch A, Kros CJ (2003) Sodium and calcium currents shape action potentials in immature mouse inner hair cells. J Physiol 552:743–761. CrossRef Medline

Marshall MR, Clark JP 3rd, Westenbroek R, Yu FH, Scheuer T, Catterall WA (2011) Functional roles of a C-terminal signaling complex of CaV1 channels and A-kinase anchoring protein 15 in brain neurons. J Biol Chem 286:12627–12639. CrossRef Medline

Meinrenken CJ, Borst JG, Sakmann B (2003) Local routes revisited: the space and time dependence of the Ca2+ signal for phasic transmitter release at the rat calyx of Held. J Physiol 547:665–689. CrossRef Medline

Michna M, Knirsch M, Hoda JC, Muenkner S, Langer P, Platzer J, Striessnig J, Engel J (2003) Cav1.3 (alpha1D) Ca2+ currents in neonatal outer hair cells of mice. J Physiol 553:747–758. CrossRef Medline

Morrison D, Schindler RA, Wersäll J (1975) A quantitative analysis of the afferent innervation of the organ of corti in guinea pig. Acta Otolaryngol 79:11–23. CrossRef Medline

Murata Y, Fujiwara Y, Kubo Y (2002) Identification of a site involved in the block by extracellular Mg(2+) and Ba(2+) as well as permeation of K(+) in the Kir2.1 K(+) channel. J Physiol 544:665–677. CrossRef Medline

Negulyaev YA, Markwardt F (2000) Block by extracellular Mg2+ of single human purinergic P2X4 receptor channels expressed in human embryonic kidney cells. Neurosci Lett 279:165–168. CrossRef Medline

Palmer AR, Russell IJ (1986) Phase-locking in the cochlear nerve of the guinea-pig and its relation to the receptor potential of inner hair-cells. Hear Res 24:1–15. CrossRef Medline

Pasic TR, Rubel EW (1989) Rapid changes in cochlear nucleus cell size following blockade of auditory nerve electrical activity in gerbils. J Comp Neurol 283:474–480. CrossRef Medline

Pérez-García MT, Kamp TJ, Marbán E (1995) Functional properties of cardiac L-type calcium channels transiently expressed in HEK293 cells. Roles of alpha 1 and beta subunits. J Gen Physiol 105:289–305. CrossRef Medline

Platzer J, Engel J, Schrott-Fischer A, Stephan K, Bova S, Chen H, Zheng H, Striessnig J (2000) Congenital deafness and sinoatrial node dysfunction in mice lacking class D L-type Ca2+ channels. Cell 102:89–97. CrossRef Medline

Rodríguez-Contreras A, Yamoah EN (2001) Direct measurement of single-channel Ca(2+) currents in bullfrog hair cells reveals two distinct channel subtypes. J Physiol 534:669–689. CrossRef Medline

Rodríguez-Contreras A, Yamoah EN (2003) Effects of permeant ion concentrations on the gating of L-type Ca2+ channels in hair cells. Biophys J 84:3457–3469. CrossRef Medline

Rodriguez-Contreras A, Nonner W, Yamoah EN (2002) Ca2+ transport properties and determinants of anomalous mole fraction effects of single voltage-gated Ca2+ channels in hair cells from bullfrog saccule. J Physiol 538:729–745. CrossRef Medline

Rodriguez-Contreras A, Lv P, Zhu J, Kim HJ, Yamoah EN (2008) Effects of strontium on the permeation and gating phenotype of calcium channels in hair cells. J Neurophysiol 100:2115–2124. CrossRef Medline

Roehm PC, Xu N, Woodson EA, Green SH, Hansen MR (2008) Membrane depolarization inhibits spiral ganglion neurite growth via activation of multiple types of voltage sensitive calcium channels and calpain. Mol Cell Neurosci 37:376–387. CrossRef Medline

Rusznák Z, Szucs G (2009) Spiral ganglion neurones: an overview of morphology, firing behaviour, ionic channels and function. Pflugers Arch 457:1303–1325. CrossRef Medline

Rusznák Z, Bakondi G, Pocsai K, Pór A, Kosztka L, Pál B, Nagy D, Szucs G (2008) Voltage-gated potassium channel (Kv) subunits expressed in the rat cochlear nucleus. J Histochem Cytochem 56:443–465. CrossRef Medline

Schnee ME, Ricci AJ (2003) Biophysical and pharmacological characterization of voltage-gated calcium currents in turtle auditory hair cells. J Physiol 549:697–717. CrossRef Medline

Spoendlin H (1981) Differentiation of cochlear afferent neurons. Acta Otolaryngol 91:451–456. CrossRef Medline

Tritsch NX, Yi E, Gale JE, Glowatzki E, Bergles DE (2007) The origin of spontaneous activity in the developing auditory system. Nature 450:50–55. CrossRef Medline

Wei D, Jin Z, Järlebark L, Scarfone E, Ulfendahl M (2007) Survival, synaptogenesis, and regeneration of adult mouse spiral ganglion neurons in vitro. Dev Neurobiol 67:108–122. CrossRef Medline

Wei D, Levic S, Nie L, Gao WQ, Petit C, Jones EG, Yamoah EN (2008) Cells of adult brain germinal zone have properties akin to hair cells and can be used to replace inner ear sensory cells after damage. Proc Natl Acad Sci U S A 105:21000–21005. CrossRef Medline

Wingo TL, Shah VN, Anderson ME, Lybrand TP, Chazin WJ, Balser JR (2004) An EF-hand in the sodium channel couples intracellular calcium to cardiac excitability. Nat Struct Mol Biol 11:219–225. CrossRef Medline

Xu W, Lipscombe D (2001) Neuronal $Ca_V 1.3\alpha_1$ L-type channels activate at relatively hyperpolarized membrane potentials and are incompletely inhibited by dihydropyridines. J Neurosci 21:5944–5951. Medline

Yamaguchi K, Ohmori H (1990) Voltage-gated and chemically gated ionic channels in the cultured cochlear ganglion neurone of the chick. J Physiol 420:185–206. Medline

Yamoah EN, Crow T (1994) Two components of calcium currents in the soma of photoreceptors of Hermissenda. J Neurophysiol 72:1327–1336. Medline

Yamoah EN, Lumpkin EA, Dumont RA, Smith PJ, Hudspeth AJ, Gillespie PG (1998) Plasma membrane Ca^{2+}-ATPase extrudes Ca^{2+} from hair cell stereocilia. J Neurosci 18:610–624. Medline

Zampini V, Johnson SL, Franz C, Lawrence ND, Münkner S, Engel J, Knipper M, Magistretti J, Masetto S, Marcotti W (2010) Elementary properties of CaV1.3 Ca(2+) channels expressed in mouse cochlear inner hair cells. J Physiol 588:187–199. CrossRef Medline

Zhang XL, Gold MS (2009) Dihydropyridine block of voltage-dependent K+ currents in rat dorsal root ganglion neurons. Neuroscience 161:184–194. CrossRef Medline